Order Number 9512571

The current-voltage characteristics of linear chains of submicron Josephson tunnel junctions

Tien, Joseph Jui, Ph.D.

University of Illinois at Urbana-Champaign, 1994

U·M·I
300 N. Zeeb Rd.
Ann Arbor, MI 48106

THE CURRENT-VOLTAGE CHARACTERISTICS OF LINEAR CHAINS OF SUBMICRON JOSEPHSON TUNNEL JUNCTIONS

BY

JOSEPH JUI TIEN

B.S., University of California, Berkeley, 1983
M.S., University of California, Los Angeles, 1985

THESIS

Submitted in partial fulfillment of the requirements
for the degree of Doctor of Philosophy in Physics
in the Graduate College of the
University of Illinois at Urbana-Champaign, 1994

Urbana, Illinois

UNIVERSITY OF ILLINOIS AT URBANA-CHAMPAIGN

THE GRADUATE COLLEGE

APRIL 1994

WE HEREBY RECOMMEND THAT THE THESIS BY

JOSEPH JUI TIEN

ENTITLED THE CURRENT-VOLTAGE CHARACTERISTICS OF LINEAR CHAINS OF SUBMICRON JOSEPHSON TUNNEL JUNCTIONS

BE ACCEPTED IN PARTIAL FULFILLMENT OF THE REQUIREMENTS FOR THE DEGREE OF DOCTOR OF PHILOSOPHY

Director of Thesis Research

Head of Department

Committee on Final Examination†

Chairperson

† Required for doctor's degree but not for master's.

O-517

The Current-Voltage Characteristics of Linear chains of
Submicron Josephson Tunnel Junctions

Joseph J. Tien, Ph.D.
Department of Physics
University of Illinois at Urbana-Champaign, 1994
Dale J. Van Harlingen, Advisor

The recent experimental results on granular superconducting films have suggested an universal sheet resistance threshold of 6.4 kΩ/square, below which all films become superconducting with decreasing temperature, and above which all films become insulating with decreasing temperature. At the critical sheet resistance of 6.4 kΩ/square, the conductance of the granular films exhibited unusual quasi-reentrant behavior with decreasing temperature.

Theories have been proposed to explain the temperature dependence of the conductance of the granular films. Most of the theories modeled the granular film as an ordered two dimensional arrays consisting of *resistively shunted Josephson junctions* (RSJ), and the inter-grain charging energy $E_c = Q^2/2C$ is responsible for the insulating behavior in high resistance films at low temperatures, and the quasi-reentrant behavior in the temperature dependence of the conductance is the result of competition between charging and Josephson effects.

The existence of disorder in granular films changes the nature of conduction at the percolation threshold from a two dimensional one, as in two dimensional arrays, to an one dimensional one, as in linear chains.

If disorder is present at the percolation threshold, the current is carried by exactly one path across the film; a *linear chain* of small superconducting gains stretching across the film. Therefore, the behavior of the granular film at the percolation threshold is strictly an one dimensional problem, and it can be modeled as a linear chain of Josephson junctions. The purpose of this thesis was to model the granular films as linear chains of

Josephson junctions and study the temperature dependence of the dynamic resistance of the chains as functions of different normal state resistances in an attempt to understand the origin of the quasi-reentrant behavior.

We have found that, although the competition between charging and Josephson effects may be one of the factors causing the observed quasi-reentrant behavior at very low temperature , it does not appear to be very important near the superconducting transition, where quasiparticle population may be significant. In addition, computer simulations on model based on competition between quasiparticle and Josephson conduction were able to reproduce most of the observed quasi-reentrant results without charging effects.

The presence of charge traps within the junctions within the chains may cause quasi-periodic switching in the dynamic resistance of the chains, causing the appearance of periodic oscillations in the dynamic resistance as temperature is lowered.

In summary, we believed the quasi-reentrant behavior in the granular films near the superconducting transition was caused by competition between quasiparticle and Josephson conduction, and not related to charging effects. In addition, the presence of charge traps can cause the measured dynamic resistance to fluctuate. If the superconducting transition temperatures of the films were inferred from transport measurements, as it was the case in the data of Goldman et. al., such fluctuations in dynamic resistance would give the appearance of superconducting temperature fluctuations.

Acknowledgments

The author acknowledges the use of the Microfabrication Facilities in the Frederick Seitz Materials Research Laboratory and the Microelectronics Laboratory in the Electrical Engineering Department for the fabrication of the submicron devices studied in this thesis. In addition, the author acknowledges the use Center of Microanalysis in the Frederick Seitz Materials Research Laboratory and the assistance of its staff in characterization of the thin films used in this work.

This work was supported by National Science Foundation under the Materials Research Laboratory grant NSF-DMR90-15-20538.

Contents

Chapter I

Introduction

I.I Josephson Junctions

A Josephson junction consists of two bulk superconductors separated by a thin layer of oxide that acts as a tunneling barrier between the bulk superconductors.

The superconducting state of the bulk superconductors can be described by an complex order parameter:

$$\Psi_{L,R} = |\Psi_{L,R}| e^{i\phi_{L,R}} \qquad \text{(I.I.1)}$$

$\Psi_{L,R}$ and $\phi_{L,R}$ are the order parameter and its phase of the superconducting condensates of the left(right) bulk superconductor making up the junction. The complex order parameter Ψ can be thought of as the " wave function" of the superconducting condensate.

If there is a difference in the phase $\phi = \phi_L - \phi_R$ between the two superconductors, a tunneling current consisting of Cooper pairs flows between the superconductors in an attempt to minimize the phase difference ϕ. The magnitude of the current is given by the Josephson relation:

$$I = I_C \sin\phi \qquad \text{(I.I.2)}$$

where I_c is the critical current of the Josephson junction. If the junction is biased by a finite voltage V, the phase difference ϕ oscillates at the frequency:

$$\frac{d\phi}{dt} = \frac{2e}{\hbar} V \tag{I.I.3}$$

The general behavior of a classical Josephson junction can be described by the *Resistively Shunted Junction Model* (RSJ)[6], where the resistance R and capacitance C of the junction are incorporated in a phenomenological lump circuit (Fig. 1). If $I(t)$ is the external bias, then the current balance gives the equation of motion for the phase difference ϕ:

$$\frac{\hbar C}{2e}\ddot{\phi} + \frac{\hbar}{2eR}\dot{\phi} + I_c \sin\phi = I(t) \tag{I.I.4}$$

The corresponding *non-dissipative* Hamiltonian becomes:

$$H = \frac{Q^2}{2C} - \frac{\hbar I_c}{2e}\cos\phi - \frac{\hbar I}{2e}\phi \tag{I.I.5}$$

The canonical variables for the Hamiltonian are $\hbar\phi/2e$ and Q. The variable Q denotes the charge of the junction. Physically, the RSJ Hamiltonian describes the dynamics of the junction as a fictitious particle of mass C moving in phase space on a washboard potential of the form (Fig. 2):

$$U(\phi) = \frac{\hbar I_c}{2e}\cos\phi - \frac{\hbar I}{2e}\phi \tag{I.I.7}$$

Within the RSJ model, the phase ϕ is treated as a c^* number. However, the canonical variables $\hbar\phi/2e$ and Q are , in reality, quantum mechanical operators satisfying an uncertainty relation of the from:

$$\Delta\left(\frac{\hbar\phi}{2e}\right)\Delta Q \le \hbar \tag{I.I.6}$$

In the classical model such as the RSJ, the quantum mechanical nature of the canonical variables are not so apparent; its effects, however, become more and more important as junction capacitance becomes smaller and smaller.

Nevertheless, the lump circuit approach, such as the RSJ model, has contributed much in the understanding of the dynamics of the Josephson junctions; it is the simplest and the most convenient way to understand the physics of the device. The shortcoming of the RSJ model is that dissipation in the equation of motion of the junction (Eq. I.I.4) can not be derived from the junction Hamiltonian (Eq. I.I.5); it has to be introduced into the equation of motion by hindsight.

Caldeira and Leggett, in an attempt to incorporate the dissipation into the Hamiltonian formalism, modeled the dissipation as a bath of harmonic oscillators with the bath Hamiltonian as:

$$H_{osc} = \sum_{\alpha} \frac{1}{2} m_{\alpha} \dot{x}_{\alpha}^2 - \sum_{\alpha} \frac{1}{2} m_{\alpha} \dot{x}_{\alpha}^2 \left(x_{\alpha} + \frac{\hbar \phi \lambda_{\alpha}}{2e m_{\alpha} \omega_{\alpha}} \right)^2 \qquad \text{(I.I.7)}$$

Where x_α, m_α, ω_α and λ_α are coordinate, mass, frequency, and coupling constant between the bath and the junction, respectively.

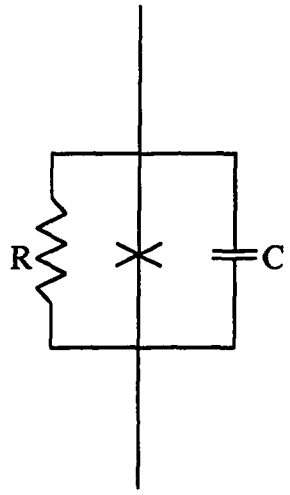

Figure 1. The resistively shunted junction model (RSJ) of a real Josephson junction in terms of ideal lump circuit elements of resistance R and capacitance , where R and C are constants.

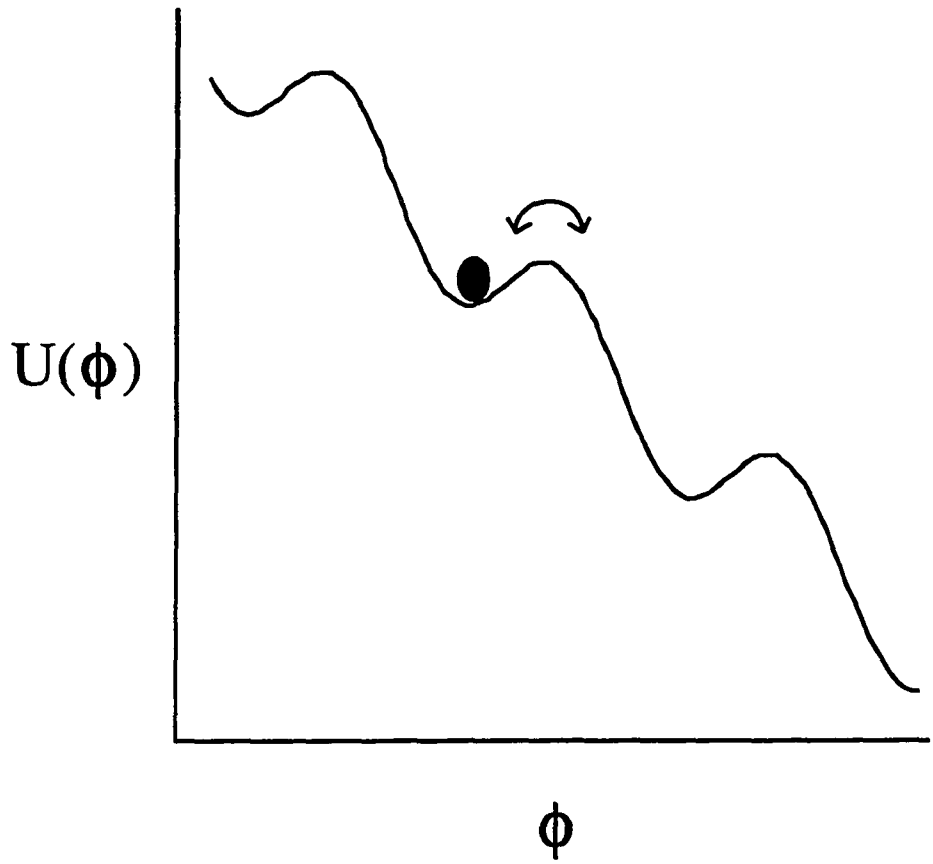

Figure 2. The RSJ washboard potential with a fictitious particle of mass $\hbar C/2e$ moving atop of it in phase space. When the particle is trapped in one of the wells, the Josephson junction is said to be in the superconducting state

I.II Charging Effects

As the size of a Josephson junction gets smaller and smaller, and the charging energy E_C of the junction becomes comparable to the Josephson coupling energy E_J, both ϕ and Q must be treated as quantum mechanical operators.

In the extreme limit of large charging energy, the charge fluctuations are totally suppressed, and the phase fluctuations becomes infinite. In this limit, the charge Q can be treated as c^* number, and the Hamiltonian at zero bias:

$$H = \frac{Q^2}{2C} - \frac{\hbar I_C}{2e}\cos\phi \qquad \text{(I.II.1)}$$

The commutation relations between the canonical variables:

$$\left[\frac{\hbar\phi}{2e}, Q\right] = i\hbar \qquad \text{(I.II.2)}$$

The above Hamiltonian maps to the problem of an electron in an one dimensional crystal, with charging energy $Q^2/2C$ as the "kinetic energy" of the particle, and the Josephson tunneling term $\hbar I_C/2e\cos\phi$ plays the role of crystal potential. The energy levels of the junction now form bands with periodicity 2e, and the "energy gap" at the edge of the zone is just the Josephson coupling energy $\hbar I_C/2e$ (Figure 3).

If we follow the lowest energy band as we increase Q, the energy of the junction oscillates with periodicity 2e. Physically, this corresponds to periodic transfer of Cooper pairs across the junction, and the voltage across the junction now oscillates with periodicity 2e. Such voltage oscillations are called *Bloch oscillations*. The canonical analogy of the Bloch oscillations is the Josephson oscillations.

The charging effect may also occur in normal tunnel junctions (Figure 3), except that the voltage across the junction is related to the phase of an electron wave function by the following integral:

$$\phi = \frac{e}{\hbar}\int_{-\infty}^{t} V(t')dt' \qquad \text{(I.II.3)}$$

The periodicity of the bands is now e instead of 2e, and the voltage oscillation is called *Single Electron tunneling* oscillations (SET).

When a tunnel junction is under current bias, the instantaneous voltage across the tunnel junction oscillates with time, such voltage oscillations is called *Bloch oscillations* if the unit charge is a Cooper pair, and *SET oscillations* if the unit charge is an electron. The time average value of the voltage oscillations yields a voltage offset in the IV characteristics of a tunnel junction. The voltage offset is known as *Coulomb blockade* (Figure 4).

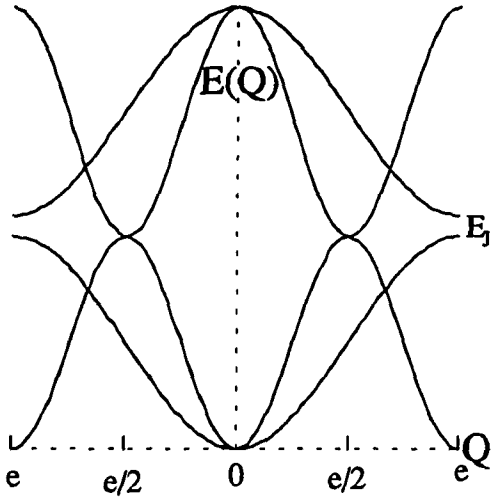

Figure 3. The band structure diagram of a ultra small Josephson tunnel junction, including single electron tunneling, in the limit of vanishing junction capacitance. The energy gap at the edge of the zone, E_J is just the Josephson coupling energy $\hbar I_C/2e$, and the band edges for Bloch and SET tunneling are at e and e/2, respectively.

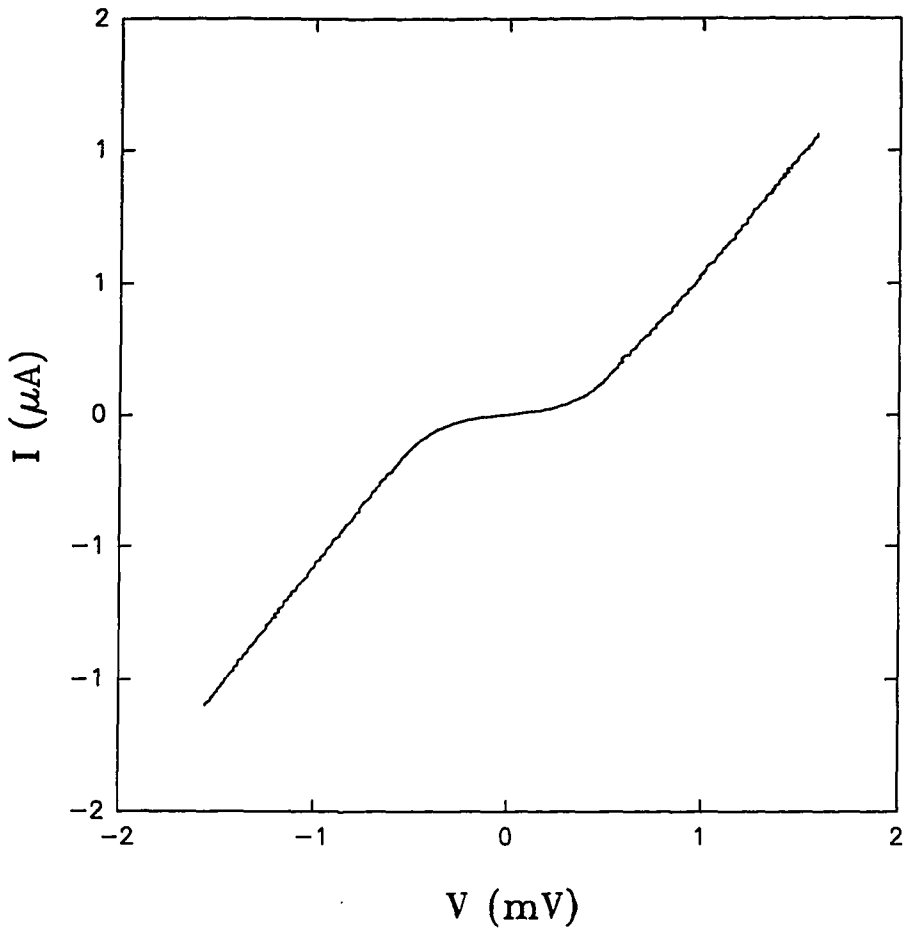

Figure 4. The IV characteristic of a normal tunnel junction at 0.4 K. The voltage offsets is the signature of Coulomb blockade.

I.III Granular Films

Recent results (Figure 5) of Orr, Jaeger Goldman and Kuper (OJGK)[1,2] on the studies of the onset of superconductivity of thin granular Sn films suggested that the only relevant parameter in determining whether the film would become superconducting was the normal state sheet resistance, R_S. The samples of OJGK were prepared by successive in-situ evaporation of Sn films onto polished Alumna substrates, which were mounted on the bottom of a He^3 cryostat. The temperature dependence of sheet resistance was measured at various film thicknesses.

For film sheet resistance less than about 6.4 KΩ/square, OJGK observed the Sn films becomes superconducting as temperature is lowered. For film sheet resistance greater than 6 KΩ/square, the films becomes insulating as temperature decreases. In thinner films with sheet resistance slightly larger than 6.4 KΩ/square, the resistance drops initially with decreasing temperature, but upon further cooling reached a plateau and started *increasing* with decreasing temperature. This quasi reentrant behavior, which had been reported in several earlier experiments[3,4], was more pronounced for larger values of R_S. The most important aspect of the OJGK result was that in each of the seven different samples, the same resistance was found to separate the superconducting and the insulating regimes. This led OJGK to suggest the existence of a universal maximum resistance threshold for thin films, above which superconductivity can not be established.

Granular films are often modeled as random networks of conducting islands (Figure 6), which are connected to other islands by high resistance links. As temperature is lowered to below T_c, the adjoining links can be considered as small Josephson junctions. The Sn films of OJGK consisted of superconducting grains of various sizes randomly distributed atop of the substrates. At the percolation threshold, there exists exactly one conduction path across the film consisting of adjoining Josephson weak links. Therefore, the behavior of the films at the percolation threshold can be modeled by a chains of Josephson weak links. In the limit of extreme disorder, the weakest link in the chain

should determine the behavior of the film. Such an assumption, known as the independent junction approach, has been used by Fisher[5] to explain the quasi reentrant behavior. The alternative approaches are to consider the granular films at the percolation threshold as either a linear chains or two dimensional ordered arrays of ultra small Josephson junctions.

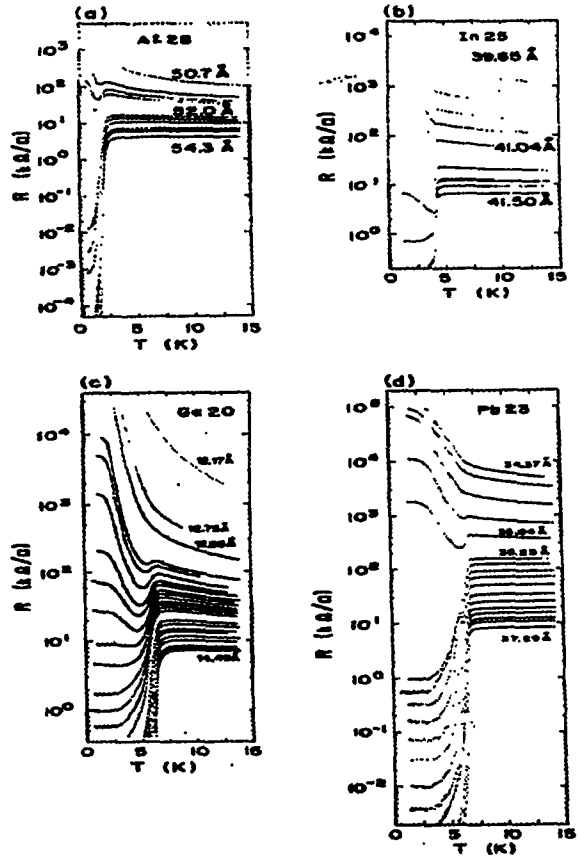

Figure 5. Resistance vs. temperature plots of various granular films. The quasi-reentrant behavior was believed to be caused by the competition between charging and Josephson effects. (Goldman et. al.)

I.IV Single Junction Model

In the RSJ model of the Josephson junction, the phase ϕ across the junction was assumed to be a classical quantity. This assumption is only true in the limit of vanishing charging energy $Q^2/2C$, where Q and C are the charge and capacitance of the junction. The dynamics of the Josephson junction is described by the RSJ equation:

$$\frac{\hbar C}{2e}\ddot{\phi}+\frac{\hbar}{2eR}\dot{\phi}+I_C\sin\phi=I(t) \qquad \text{(I.IV.1)}$$

and the corresponding washboard Hamiltonian:

$$H=\frac{Q^2}{2C}-\frac{\hbar I_C}{2e}\cos\phi-\frac{\hbar I}{2e}\phi \qquad \text{(I.IV.2)}$$

Where all variables have their usual meanings.

When device becomes smaller, charging energy $Q^2/2C$ becomes significant and the phase ϕ becomes an quantum mechanical operator. In the extreme quantum limit, charge and phase satisfy the commutation relation:

$$\left[\frac{\hbar\phi}{2e}Q\right]=i\hbar \qquad \text{(I.IV.3)}$$

It is apparent that the form of equation (III.2.1) is not time reversal invariant due to the inherent dissipation in the shunt resistor R. The generalization of the Hamiltonian (I.IV.2) to the fully quantum mechanical case and to incorporate dissipation within the Hamiltonian formalism was not altogether straight forward.

The problem was solved by Caldeira and Leggett, who modeled dissipation by coupling the phase ϕ to a bath of harmonic oscillators with infinite degrees of freedoms. The Hamiltonian is given as

$$H=\frac{1}{2C}\left[2en+\int_0^t I(t')dt'+\sum_\alpha \lambda_\alpha x_\alpha\right]^2-E_J\cos\phi+H_{osc} \qquad \text{(I.IV.4)}$$

with

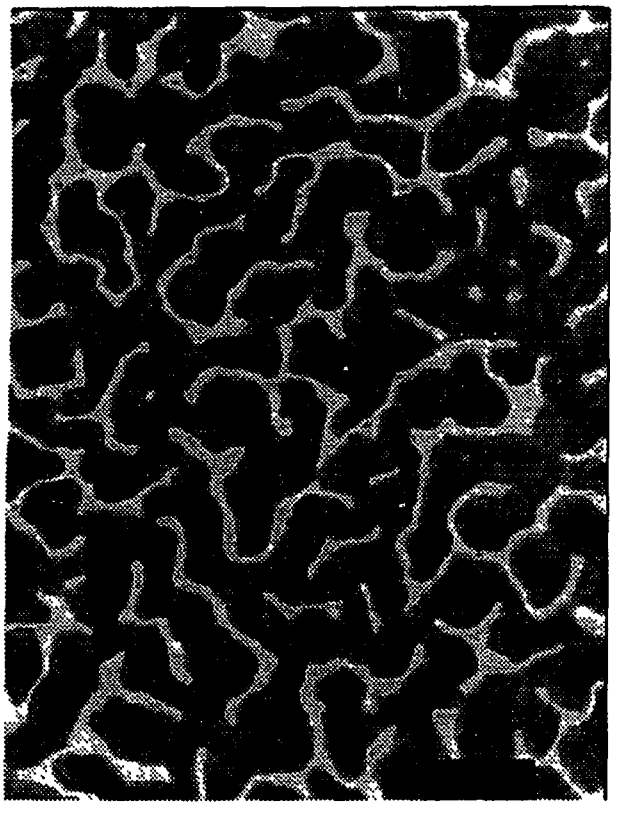

Figure 6. The topology of granular Pb film on top of Ge near the percolation threshold. The topology suggests the presence of minimum number of paths available for conduction.

$$I_N = -\sum_\alpha \lambda_\alpha \dot{x}_\alpha \tag{I.IV.5}$$

and

$$H_{osc} = \sum_\alpha \frac{1}{2} m_\alpha \dot{x}_\alpha^2 - \sum_\alpha \frac{1}{2} m_\alpha \dot{x}_\alpha^2 \left(x_\alpha + \frac{\hbar \phi \lambda_\alpha}{2e m_\alpha \omega_\alpha} \right)^2 \tag{I.IV.6}$$

where I_N is the normal current of the junction. The particle coordinate ϕ is coupled to a bath of harmonic oscillators of mass m_α and frequency ω_α with the Hamiltonian H_{osc} . The parameters $\{x_\alpha\}$ and $\{\lambda_\alpha\}$ are coordinates and coupling constants of the harmonic oscillators, respectively.

The CL Lagrangian is not invariant with respect to 2π translation of the phase ϕ. This lack of invariance is not a major difficulty if fluctuations of ϕ is small with respective to 2π. If the phase fluctuations is not small with respect to 2π, a more suitable Lagrangian is needed.

Fisher and coworkers has proposed a modified Lagrangian that is manifestly invariant with 2π translation. The Lagrangian has the form

$$\begin{aligned} L = & \frac{1}{2C}\left(\frac{\hbar C}{2e}\right)^2 \dot{\phi}^2 + E_J \cos\phi - \frac{\hbar \dot{\phi}}{2e}\left(\int_0^t I(t')dt' + \sum_\alpha \lambda_\alpha x_\alpha \right) \\ & \sum_\alpha \frac{1}{2} m_\alpha \dot{x}_\alpha^2 - \sum_\alpha \frac{1}{2} m_\alpha \omega_\alpha^2 \left(x_\alpha + \frac{\lambda_\alpha \hbar \phi}{2e m_\alpha \omega_\alpha} \right)^2 \end{aligned} \tag{I.IV.11}$$

The Lagrangian given above is formally equivalent to the Caldeira-Leggett Lagrangian for a particle moving on a washboard potential. Schmid was the first to point out that this problem is similar to a particle hopping on a one dimensional tight binding lattice coupling to a dissipative environment, and there exist an interesting self-duality. The self duality of the model leads to a zero temperature phase diagram with two distinct regimes separated by a critical value of shunt resistance R_S . When R_S is less than the

quantum resistance R_Q of 6.4 KΩ, the phase ϕ is delocalized, and the junction is superconducting. When R_S is greater than 6.4 KΩ, the phase ϕ is localized, and the junction is normal.

The zero-temperature phase diagram of such dissipative transition has been derived by Fisher. The phase transition of the system manifests itself in the symmetry of the ground state wave function.When R_S is larger than the quantum resistance R_Q of 6.4 KΩ, the ground state wave function of the fictitious particle in phase is invariant with respect to discrete translation of the phase ($\phi \rightarrow \phi + 2\pi$). The states at ϕ and $\phi \rightarrow \phi + 2\pi$ can no longer be treated as distinguishable states, and the junction exhibits finite resistance. When R_S is less than the quantum resistance R_Q of 6.4 KΩ, there is symmetry breaking; the ground state wave function no longer respects the discrete translational symmetry of the Hamiltonian and the ground state wave function is localized in phase space; the junction is now superconducting and has zero resistance.

In summary, the phase transition is consequence of the localization-delocalization of the phase ϕ, and its location depends only on the value of the shunt resistance R_S; it is independent of either the Josephson coupling energy E_J or the junction capacitance C. At absolute zero, when the shunt resistance R_S is less than 6.4 KΩ, all the current in the junction is carried by Cooper pairs and the junction resistance is zero. When shunt resistance R_S is larger than 6.4 KΩ, all the current flows through the shunt resistor and the junction resistance is equal to the shunt resistance R_S.

Physically, one can understand these results in terms of tunneling of the phase ϕ. If the shunt resistance R_S is less than 6.4 KΩ, the phase ϕ is delocalized and tunnels by 2π between adjacent minima on the washboard potential. The tunneling of the phase induces a voltage ($V = \hbar\dot{\phi}/2e$) across the junction. The voltage V drives a small current across the shunt resistor. The charge transferred is

$$\delta Q = R_S^{-1} \int dt \left(\frac{\hbar \dot{\phi}}{2e} \right) \qquad \text{(I.IV.12)}$$

Integrating over one cycle, and noting the definition of quantum resistance R_Q

$$\delta Q = R_S^{-1} \frac{2eh}{(2e)^2} = 2e \frac{R_Q}{R_S} \qquad \text{(I.IV.13)}$$

Therefore, a charge at the junction can either remain on the junction electrode, be carried away by Cooper pairs in units of 2e, or by normal current in unit of $2e(R_Q/R_S)$ with 2π phase slip across the junction. Since all charge transfer across the junction must overcome the charging energy barrier E_C, the dynamics of the junction acts to keep the charging energy to a minimum by passing charge in smallest possible units. When shunt resistance R_S is greater than quantum resistance R_Q, Cooper pairs carry the current in the junction. When shunt resistance R_S is less than quantum resistance R_Q, it becomes more favorable energetically for the current to flow through the shunt resistor instead of the junction, and the Cooper pairs no longer contributes to the conduction. The quantum resistance R_Q separates the two distinct regimes of conduction.

I.V Linear Chain Model

The other approach to thinking about the behavior of granular films at the percolation threshold is to consider a chain of small tunnel junctions.

Bradley et. al. has considered a case of a linear chain of ultra small Josephson tunnel junctions without dissipation. They found that when the junction self-charging energy is taken into consideration, the SI transition can be described within the framework of the Kosterlitz-Thouless (KT) transition if the Lagrangian can be mapped to the x-y model. The two relevant dimensions in this case are the phase of the Josephson junction and the imaginary time. The SI transition is the direct consequence of the competition between charging and Josephson effects.

Bobbert et. al. of Delft has extended the study of the chains by including ohmic dissipation. They have also mapped the problem to a 2D XY model with phase and imaginary time as the relevant dimensions. This model also yield a critical resistance threshold and a phase diagram that predicts re-entrant superconductivity. The unusual aspect of the model is that it predicts two different superconducting states with two different local superconducting properties characterize by different topological arrangements of the 2π phase slips along the chain.

Although the details of both models differ, both suggest that competition between charging and Josephson effects are the cause of SI transition. When dissipation is included, there exist some type of dissipative transition responsible for the re-entrant superconductivity.

The quasiparticle conduction in the Josephson junction were not considered in both models.

I.VI Two Dimensional Arrays

Two dimensional arrays of Josephson junctions have always been considered to be a good candidate for modeling the behavior of granular films.

Since the initial experimental work of Orr et. al., there has been a quite a few theoretical works based on the ordered RSJ Josephson arrays. (Zwerger, Charkavarty, Ingold, Kivelson, Zimanyi, Schön). Although the details of the calculations differ, all of the theories based on the ordered RSJ Josephson junction arrays derived a phase diagram suggesting the existence of re-entrant superconductivity and the dissipative phase transitions. In addition, all of the theories suggest the dissipative transition occurs at the universal resistance threshold of 6.4 $K\Omega$, in perfect agreement with the observed experimental value.

I.V Summary

Recent theoretical efforts have modeled the superconducting granular film as single junction, linear chain, or two dimensional Josephson junction array. In all cases, all of the theoretical efforts, with the exception of the work of Bradley et. al., which predates the experimental result, have managed to reproduce the universal resistance threshold of 6.4 KΩ/square, in perfect agreement with the observed experimental result.

However, the underlying common denominator amongst all the theories is the competition between two conduction channels with opposite temperature dependences: the charging energy of the Josephson junction tends to suppress tunneling with decreasing temperatures, whereas the Josephson coupling energy of the junction tends to enhances the tunneling rates with decreasing temperatures. The result of such competition gives the appearance of reentrant superconductivity.

Chapter II

Device Fabrication

II.I Introduction

All microfabrication processes start with a substrate coated with resist materials being exposed to a radiation source, and forming the patterns. Depending on the radiation and type of resist to be used, we characterize the processes as optical, X-ray or electron beam lithography. In order to form useful patterns with lithography, certain important parameters in the processes have to be closely controlled, irrespective of the kinds of lithography used to define the pattern. The most important parameters are summarized below:

τ = pixel exposure time (sec)

D = area dose (C/cm^2)

fD = dose per pixel ($f \leq 1$)

l_p^2 = pixel area (cm^2)

l_p^2/τ = area exposed per second (cm^2/sec)

j = current density per pixel (amp/cm^2)

From simple dimensional analysis, one can see the parameters are not independent of each other. The two most basic relationships are:

$$\frac{1}{\tau} = \frac{j}{fD} \qquad \text{(II.I.1)}$$

and

$$\frac{l_p^2}{\tau} = \frac{jl_p^2}{fD} \qquad \text{(II.I.2)}$$

Although these parameters and their relationships with respect to each other are not very important in contact optical lithography, control of these parameters and optics of the electron beam systems, however, may be the difference between success and failures in electron beam lithography.

In addition, the properties of the resists and their developers are also important in determining the ultimate resolution of the electron beam lithography system. A considerable amount of work has been published in the literature on the topic of the chemistry, solubility and the physical properties of the resists in an attempt to understand the chemistry of lithographic processes.

I shall give a brief introduction to the various lithographic systems and the basics of the resist processes relevant to the work done in this thesis. For a complete description of the topic, readers are refer to the vast body of works in the published literatures.

II.II Lithographic Pattern Formation

Lithography can be devided into three types: contact printing, projection printing, and direct writing. Of the three mentioned above, contact printing is the oldest and the simplest method, followed by projection printing; direct writing was not feasible until the advent of the electronic computers.

In contact printing, a mask containing the circuit patterns is positioned on top of the resist-covered wafer and then exposed to ultraviolet light, creating exposed and unexposed areas, and subsequent development of the exposed resist yields the desired circuit patterns. The advantage of contact printing is its simplicity. However, because contact printing exerts considerable pressure on the mask-substrate combination during printing, mask defects accumulated during successive mask use, and old masks have to be replaced by new masks over time. Other variants such as proximity printing, where mask

was moved slightly away from the surface of the substrate during printing. However, diffraction effects caused reduction in the resolution and increase distortion in the patterns, making the technique impractical for any features smaller than 7 μm.

Projecting printing was developed primarily to circumvent the mask defect problem. Because image of the circuit patterns are projected by an optical system onto the substrates, the mask need never touch the substrate. The resolution of the projection systems are often determined by the diffraction limit of their lens systems. Both optical and electron beam projection printers have been built over the years. However, only the optical projection printers have been reliable enough to be built in significant numbers. There are some electron beam projection printers in existence that can achieve 0.1 μm resolution. However, electromagnetic lenses suffered badly from spherical and geometric aberrations comparing to its optical cousins. As a result, most projection printers are optical printers.

Instead of projecting the mask patterns onto a substrate, as it is the case in projection systems, one can just raster the incident radiation to produce patterns on the substrate. With the advent of the electronic computers, the raster system with finely focused beams has gained popularity in recent years. Because the patterns in the raster system are generated from a database stored on the computer, no masks are needed. Since the database of the patterns can be change at will, this makes the raster system considerably more flexible than any mask-based systems. The main disadvantages of raster systems are increased complexity and long exposure times.

A electron raster system consists of the following basic components:

- The microscope column
- Beam shaping system
- Pattern generation system
- Sample stage

The microscope column houses the electron optics used to focus and deflect the electron beam during exposure and imaging applications. The beam shaping system usually

consists of one or more apertures and compensator coils situated at various strategic spots along the column to shape the beam traveling down the column. The pattern generating system usually consists of a pattern database stored within a digital computer with analog outputs connected to the scan generators of the microscope; the computer reads the pattern database and directs the electron beam to write the patterns onto a wafer. The sample stage is where the wafer resides; it has a xy axis translational and z axis rotation in order to facilitate optimal sample alignments.

In a standard scanning electron microscope, the column optics consists of an objective lens, a condenser lens, and a condenser aperture. The work for this thesis was done on a modified JEOL 35C scanning electron microscope with an unique 3 lens column (Figure 8). Although the presence of the additional objective lens aperture and the intermediate lens complicates the operations and the alignments of the microscope considerably, the errors and aberrations associated with the presence of the additional components were actually negligible, provided that certain precautions were taken to minimize the effects of the intermediate lens.

One of the most important parameters determining the ultimate resolution of the scanning electron beam system is the spot size of the electron beam. The spot size depends critically on the beam cross section at the first crossover and the column optics. The expression below relates the final spot size of the beam at the sample plane to the various factors affecting it:

$$d^2 = d_0^2 + d_s^2 + d_c^2 \qquad \text{(II.II.4)}$$

Where d, d_S, and d_C are the total spot size, spot size at the first crossover, diameter of the circle of least confusion caused by spherical aberration, and diameter of the circle of least confusion caused by chromatic aberration, respectively.

The spot size d_0 at the first crossover is givens as follows:

$$d_0 = \sqrt{\frac{I}{0.15\pi^2 B\alpha^2}} \qquad \text{(II.II.5)}$$

Where I is the current of the beam, B is the current density per unit solid angle, and α is the convergence angle at the sample plane.

Spherical aberrations can be characterized by the following expression:

$$d_s = \frac{\alpha^3}{2C_s} \qquad \text{(II.II.6)}$$

Where d_S is diameter of the circle of least confusion caused by the spiracle aberration, C_S is the spherical aberration constant of the condenser lens, and α is the angle of convergence of the electron beam at the sample plane.

Chromatic aberration of the lens can be characterized by the following expression:

$$d_c = C_c \frac{\Delta V}{V} \alpha \qquad \text{(II.II.7)}$$

Where d_C is the diameter of the circle of least confusion caused by the chromatic aberration, C_C is the chromatic aberration constant of the condenser lens, α is the angle of convergence of the electron beam at the sample plane, V is the incident energy of the electron, and ΔV is the effective energy spread of the incident electron beam.

Together, the expression for the final spot size at the sample plane is given as follows:

$$d^2 = \frac{I}{0.15\pi^2 B}\alpha^{-2} + \frac{C_s^2\alpha^6}{4} + \left(C_c \frac{\Delta V}{V}\right)^2 \alpha^2 \qquad \text{(II.II.8)}$$

As one can readily see from the above expression, there exist an optimal value of α that minimizes the spot size. For a well designed system, the values of C_S and C_C are usually the order of the focal lengths of the lenses, and the stability of the source ΔV should be within 5 volts.

It is interesting to note that the spot size increases as 6th power of the convergence angle α. In other words, spot size is most effectively minimized by decreasing the convergence angle of the lens. This fact has an important consequence on electron beam writing on the three-lens system such as the JEOL 35C; minimizing the

convergence angle of the intermediate lens on the JEOL 35C by de-exciting the intermediate lens, the effects of most of the aberrations from the intermediate lens can be minimized. In addition, most of the well designed objective lenses in modern microscopes are expected to operate with small convergence angle anyway. Therefore, the errors associated with the intermediate lens and objective lens can be ignored.

II.III Electron Beam Resists

An electron beam resist is basically a long chain polymer dissolved in a volatile solvent, usually chlorobenzene.

There are two basic kinds of electron beam resists: positive and negative. Positive resists breaks down into monomers of lower molecular weights upon exposure to incident electrons; negative electron beam resists cross-link when exposed to electron beams. In general, positive electron beam resists are more widely used than negative resists, primarily because positive electron beam resists tend to have a slightly higher resolution than the negative resists. Of the various positive electron beam resists that have been tried, the most common electron beam resists in electron beam lithography is Polymethymethacrylate (PMMA), otherwise known as Plexi Glass.

A positive electron beam resist is characterized by a reduction in molecular weight due to chain scission of the original molecules. Since molecules with lower molecular weights have a higher solubility in developers than the original molecular weight. The relationship between the original molecular weight M_O, and M_f, the molecular weight after chain scission can be written as follows:

$$M_f = \frac{M_o}{1 + \frac{G_e M_o \varepsilon}{100 \rho N_a}} \qquad \text{(II.III.1)}$$

Where ε is the absorbed energy density of the PMMA, ρ is the density of the PMMA, N_a is the Avogadro number, and G_e is defined as the radiation yield per 100 eV of incident electron energy.

The solubility of PMMA is given by the following empirical expression[8]:

$$R = R_0 + \frac{\beta}{M_f^{\alpha}} \qquad \text{(II.III.2)}$$

Where R is the solubility rate of PMMA in the developers, and R_0, β, and α are empirical parameters depending on temperature and types of PMMA developers.

From the above two expressions, one can get a quick determinations of the theoretical development time of the PMMA from the following expression:

$$\tau = \int_0^d \frac{1}{\left| R_0 + \frac{\beta}{M_f^{\alpha}} \right|} \qquad \text{(II.III.3)}$$

Where τ is the approximate development time, and d is the thickness of the resist. The density of PMMA is 1.2 g/cm^3, $M_0 \approx 100000$, $G_e \approx 1.9$, and $\beta \approx 1$, giving $\tau \approx 30$ seconds.

However, because the values of the empirical parameters are often unknown themselves, equation (II.III.3) is of limited utility under real laboratory conditions. In the real world of electron beam lithography, the development time τ of a working resist must be measured in the laboratory (Equation II.IV.2).

In addition to the development time τ, the two other important parameters that characterizes an electron beam resist are dosage D and contrast γ. Dosage is given by the following expressions:

$$D = \frac{it}{A} \qquad \text{(II.III.4)}$$

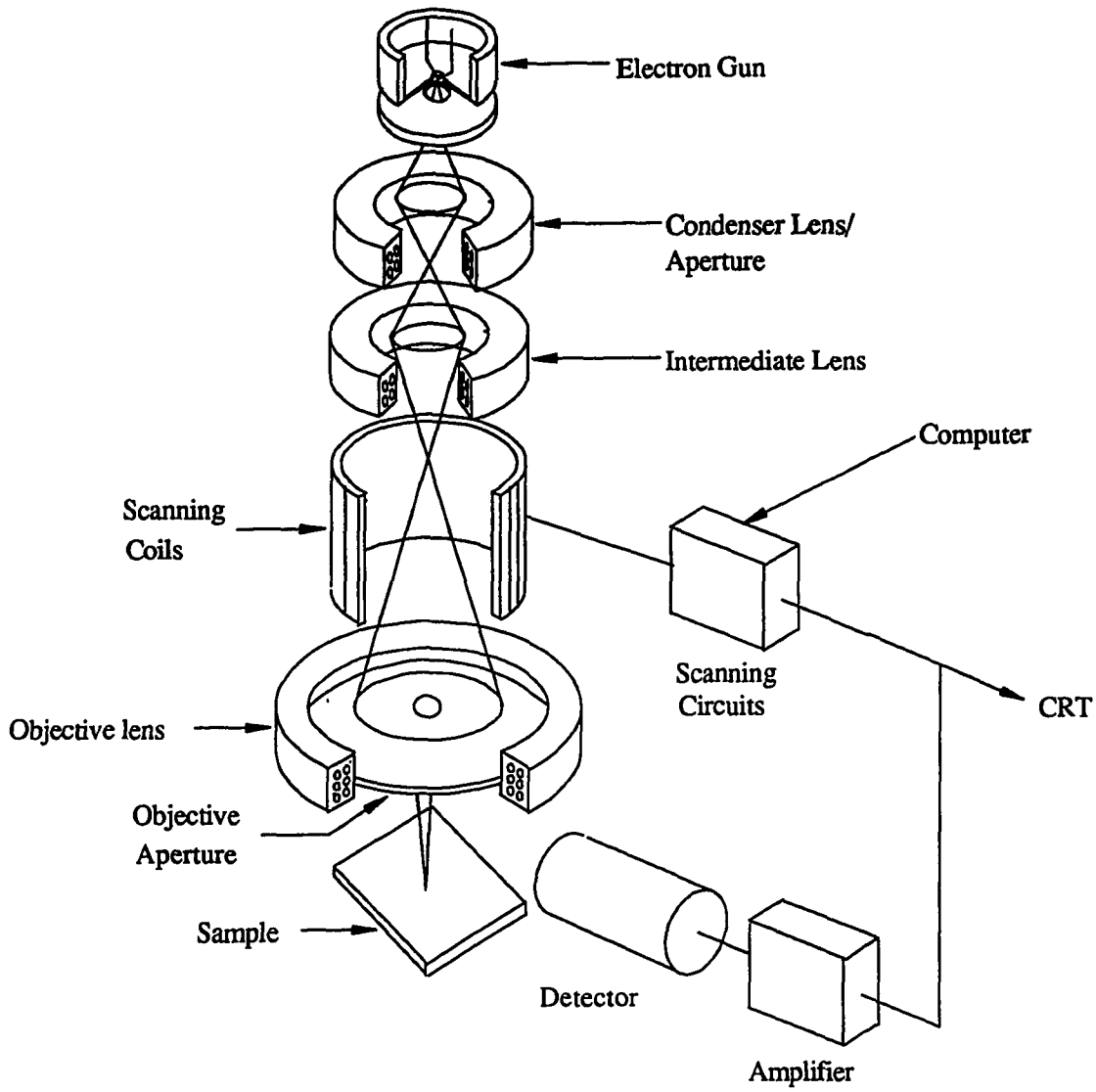

Figure 8. The general layout of the JEOL-35C SEM with its unique 3-lens column.

Where i, t, and A are the current, time, and area of the exposed resist. The contrast γ is given by the following expression:

$$\gamma = \left| \log\left(\frac{D^o}{D_m}\right) \right|^{-1} \qquad \text{(II.III.5)}$$

Where D^o is defined as the threshold dosage required to expose the resist, and D_m is the minimum dosage to completely expose the resist. The value of the γ is just the slope of the exposure curve in the linear regime; γ has a value of 1.6 for PMMA. The value of γ happens to be a very important parameter in electron beam lithography. It is the prevailed opinion that resists capable of sub micron resolution have γ equal or greater than 1. The parameter γ is also referred to as the resolution of the resist.

The development time, dosage, and contrast completely defines the working properties of the resist. A considerable amount of work in this thesis has been devoted in determination of these parameters for various operating conditions.

II.IV Resist Development

An ideal developer is the developer with the highest solubility ratio between the irradiated and the irradiated areas of the resist. Once the solubility ratio is determined, most of the work is carried to determine the minimum dosage required to irradiated the resist in order to insure complete removal of the resist at development. The solubility rate of a positive resist is proportional to the dosage:

$$R \propto D^{\alpha} \qquad \text{(II.IV.1)}$$

Where R is the solubility rate of the irradiated portion of the resist, D is the charge dose received at the irradiated areas, and α is the exponent. The value of α depends on type of the solvent used and the temperature of the solvent. For pure MIBK [1], value of α was

[1] Methy Isobutyl Ketone

experimentally determined to be about 1.5. The value of α can often be increased by judicious dilution of the MIBK with other polar solvents. However, the apparent increase in the sensitivity of the resist is achieved at the expense of the reduced resolution of the resist[9,10,11].

Because of the nature of the electron beam writer used for this work, where a local oscillator drives both the electron beam writer and both the x and y scan generators, it is more convenient to define equation (II.4.1) in terms of oscillator frequency f:

$$\tau = \kappa f^{\sigma} \qquad \text{(II.IV.2)}$$

Where κ and σ are fitting parameters for the development time τ, and f is the local oscillator frequency. The results of the calibrations for the P(MMA/MAA) system is presented at the end of this chapter.

The procedure of obtaining the ratio of the development times was relatively straight forward, if not tedious: each of the samples used in the developments were exposed with a known dosage, and the samples are subsequently developed with a fixed amount of time. The samples were subsequently cleaved and coated with gold. The depth profiles of the developed resists were imaged and measured on the Hitachi S800 scanning electron microscope.

II.V Multilayer Resists

In the past decade, many have recognized that the resolution limits that were considered to be intrinsic to the resists are not fundamental to the exposure process, but as a result of the use of single layer resist chosen to satisfy conflicting requirements.

A resist has to be thick enough to cover all the topographical features on the substrate, but it has to be thin enough to retain the required resolution. At the same time, resist has to have enough sensitivity for the incident electron beam to register the pattern onto the resist, but it has to be relatively insensitive to back scatter electrons to retain its resolution. A resist has to be relatively thin to minimize sideward development during

development, but it also thick enough to minimize standing wave effects. It is this set of conflicting requirements that allowed researchers in the field to find better solutions.

The conflicting requirements of the electron beam resists have led many people to use more than one layer of resists for exposure. The multilayer resist systems have a real advantage over the single layer resist systems: the properties of each layer can be optimized to satisfy a smaller set of requirements. For example, in a double layer electron beam resist system, the lower layer can be optimized for coverage and absorb the secondary electrons while the upper layer for resolution. However, the tradeoff is that the layers chosen have to be chemically and physically compatible with each other throughout the processes. In addition, the requirements for each of the layers must not be in conflict with other layers.

The multilayer resist used for this work consists of two layers. The top layer consists of diluted PMMA in chlorobenzene, and the bottom layer consists of P(MMA/MAA)[2], a copolymer of the PMMA. P(MMA/MAA) also has a slightly higher viscosity than PMMA when prepared; it also has the advantage of being considerable more sensitive to electrons than PMMA, making it as the ideal lower layer of the system.

When developed, the higher sensitivity of the P(MMA/MAA) will yield an undercut profile, a distinct advantage during the lift-off. Another advantage of P(MMA/MAA) is the slightly higher molecular dipole moment of the carboxyl group, making it insoluble in PMMA/chlorobenzene solution. Because P(MMA/MAA) is insoluble in PMMA/chlorobenzene, the buffer layer between PMMA and P(MMA/MAA) is no longer required.

The calibration figures for the P(MMA/MAA) system are presented at the end of this chapter.

---

[2]Polymethyl methacrylic acid

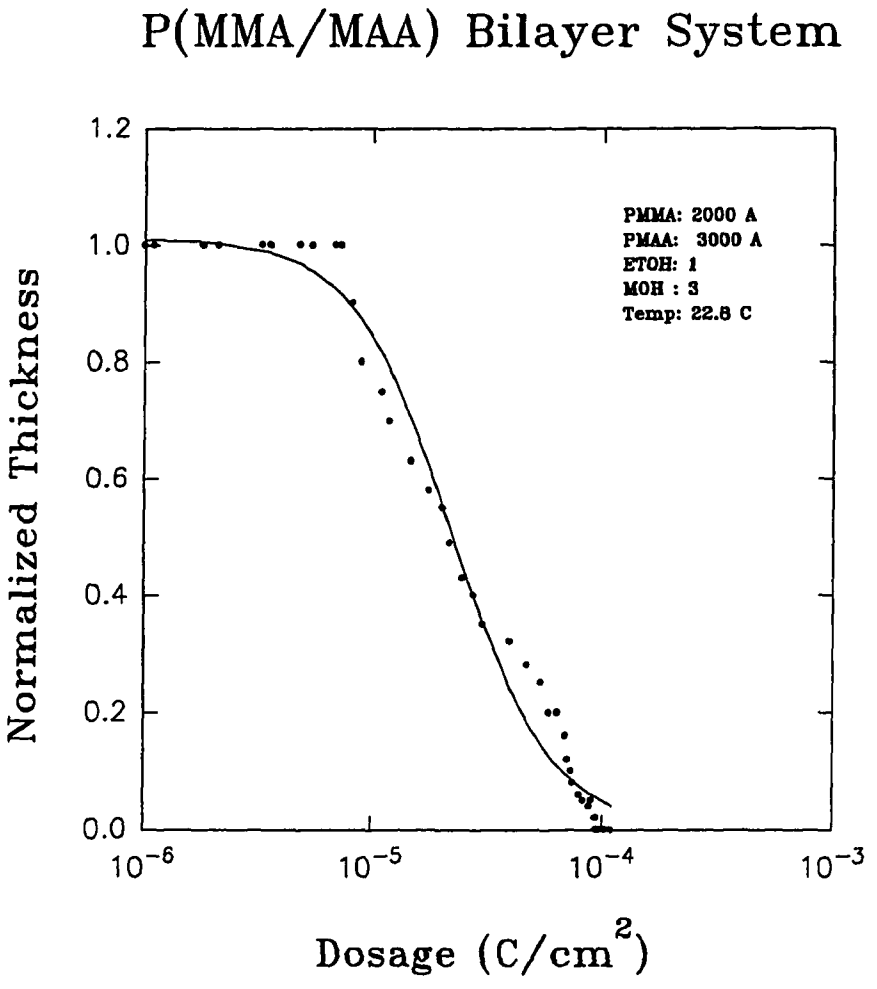

Figure 9. Dosage profile for 2000 Å PMMA atop of 3000 Å of P(MMA/MAA).

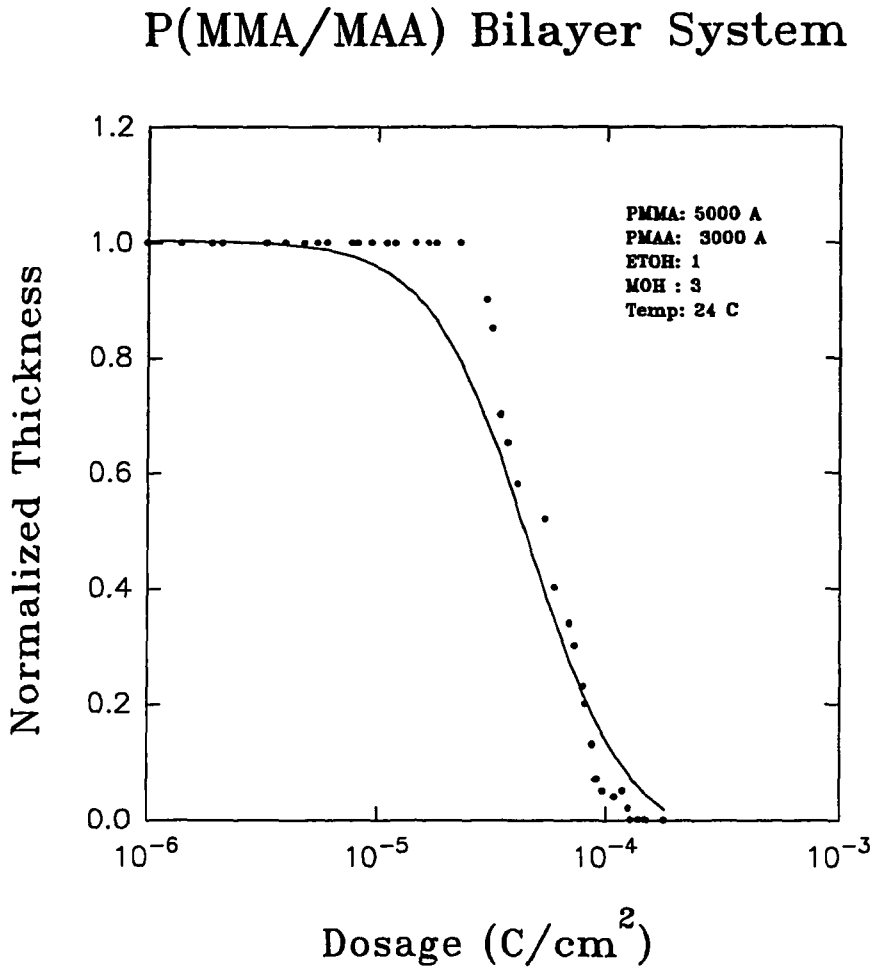

Figure 10. Dosage profile for 5000 Å PMMA atop of 3000 Å of P(MMA/MAA).

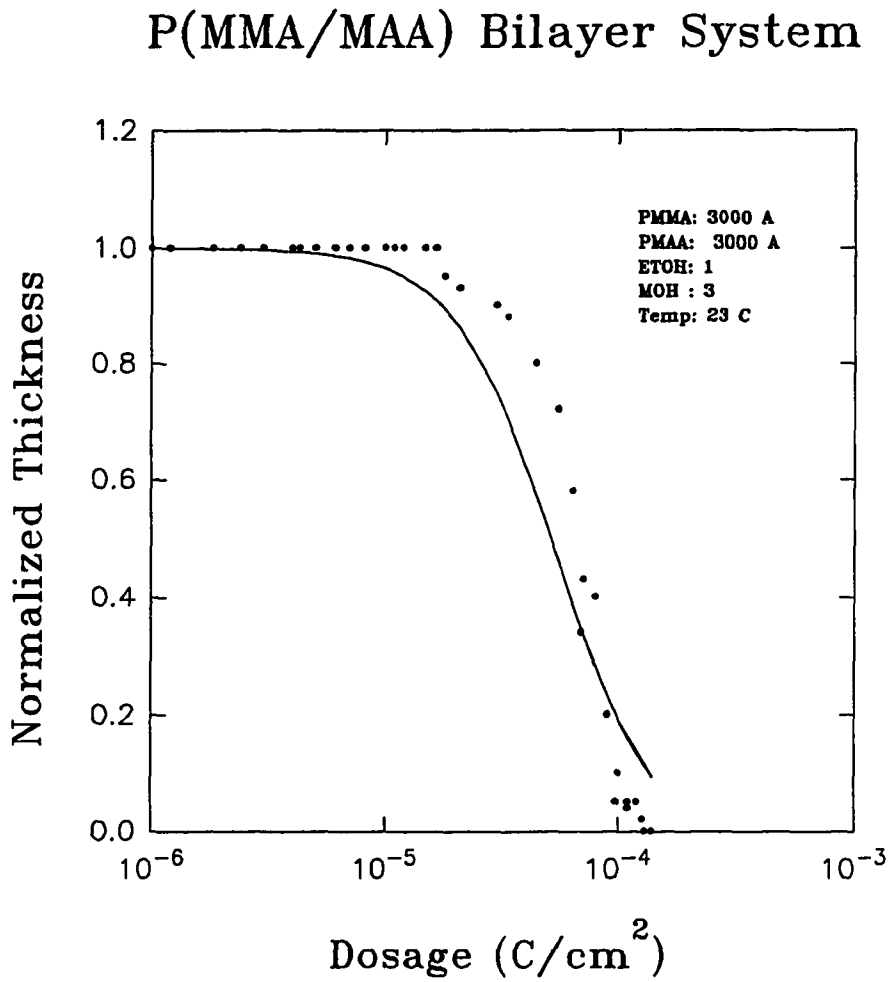

Figure 11. Dosage profile for 3000 Å PMMA atop of 3000 Å of P(MMA/MAA).

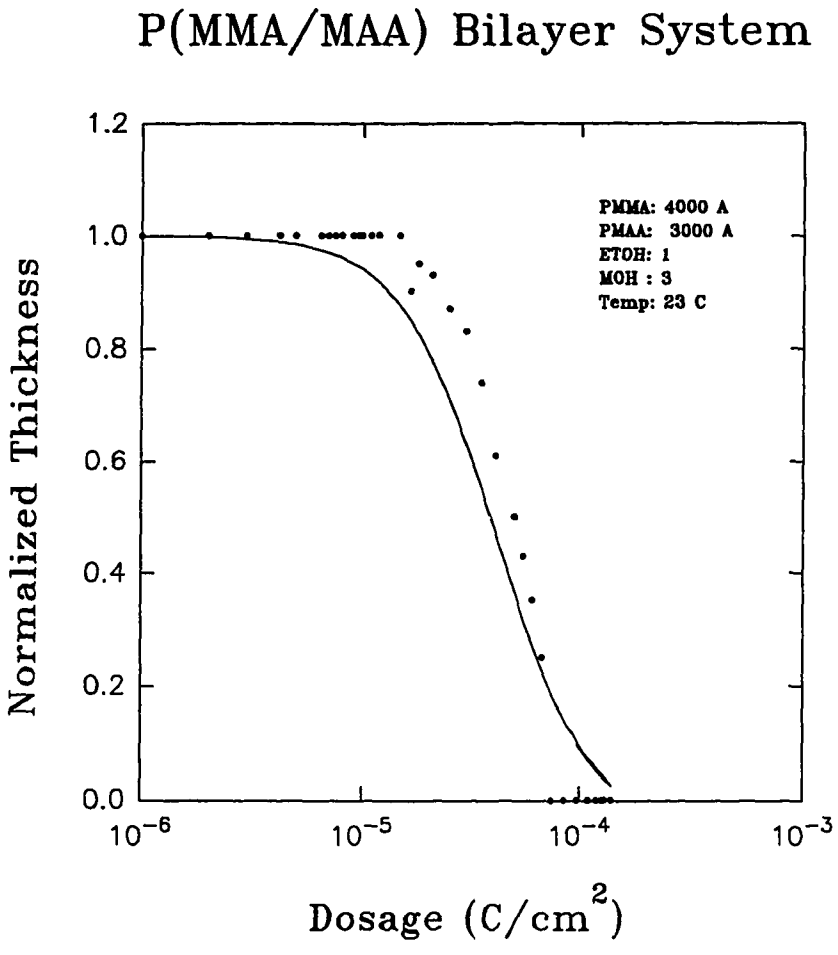

Figure 12. Dosage profile for 4000 Å PMMA atop of 3000 Å of P(MMA/MAA).

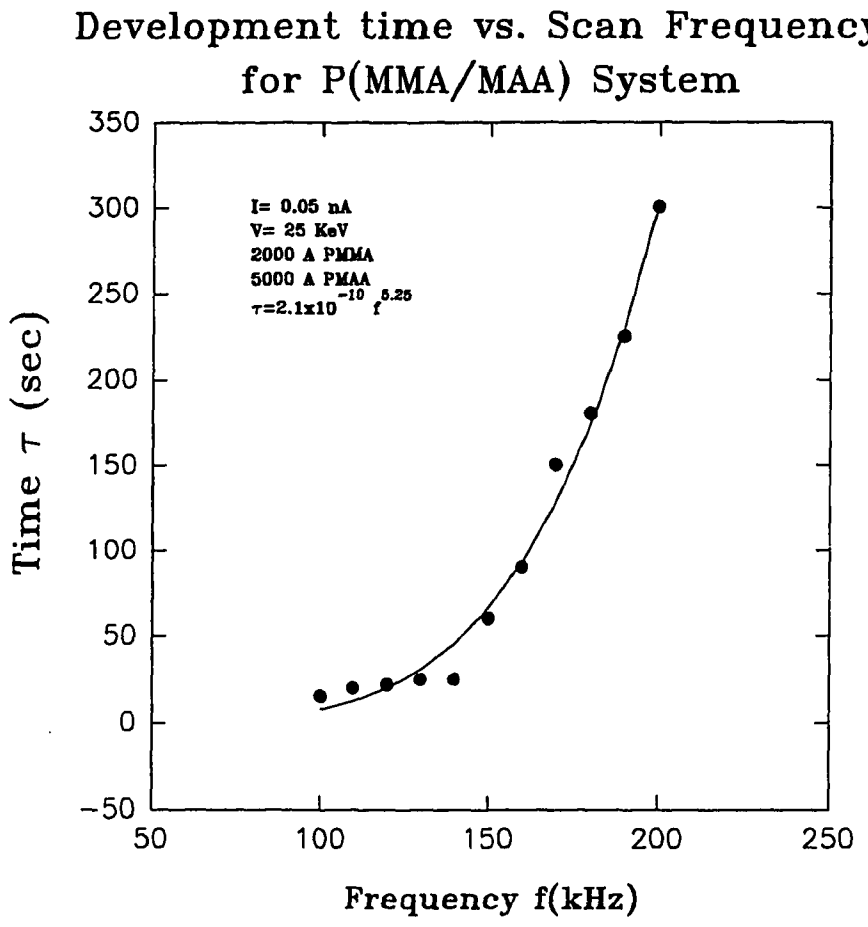

Figure 13. Development time versus scan frequency for 2000 Å PMMA atop of 5000 Å of P(MMA/MAA) at 0.05 nA beam current.

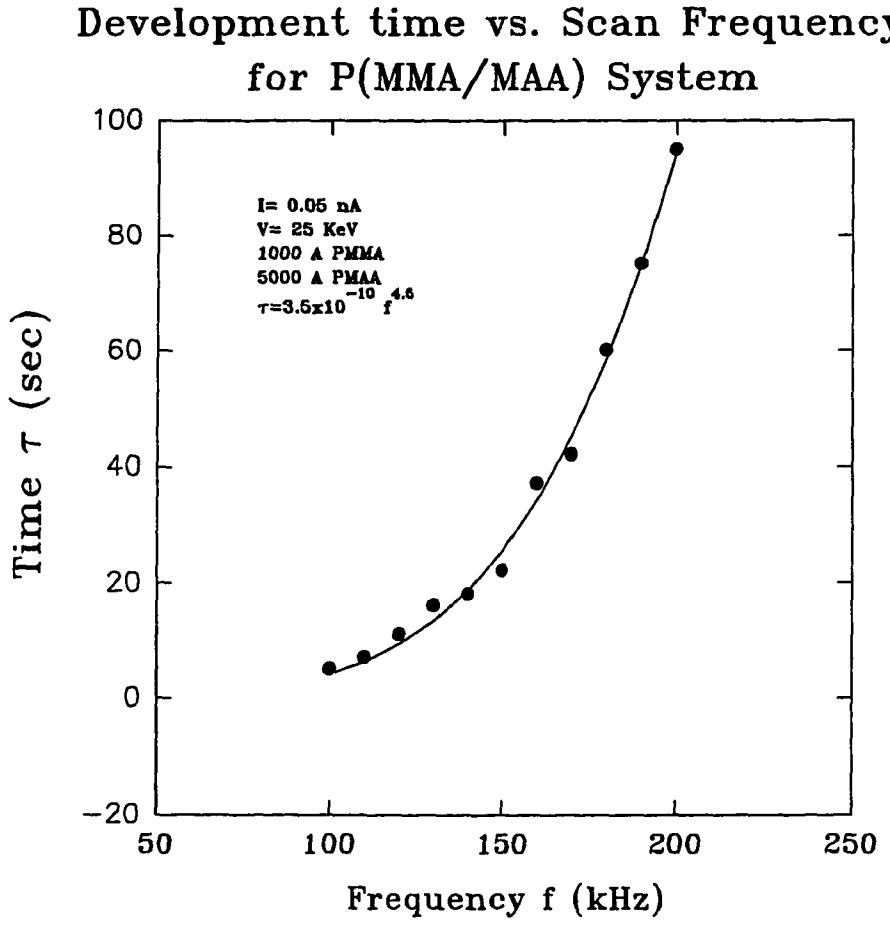

Figure 14. Development time versus scan frequency for 1000 Å PMMA atop of 5000 Å of P(MMA/MAA).

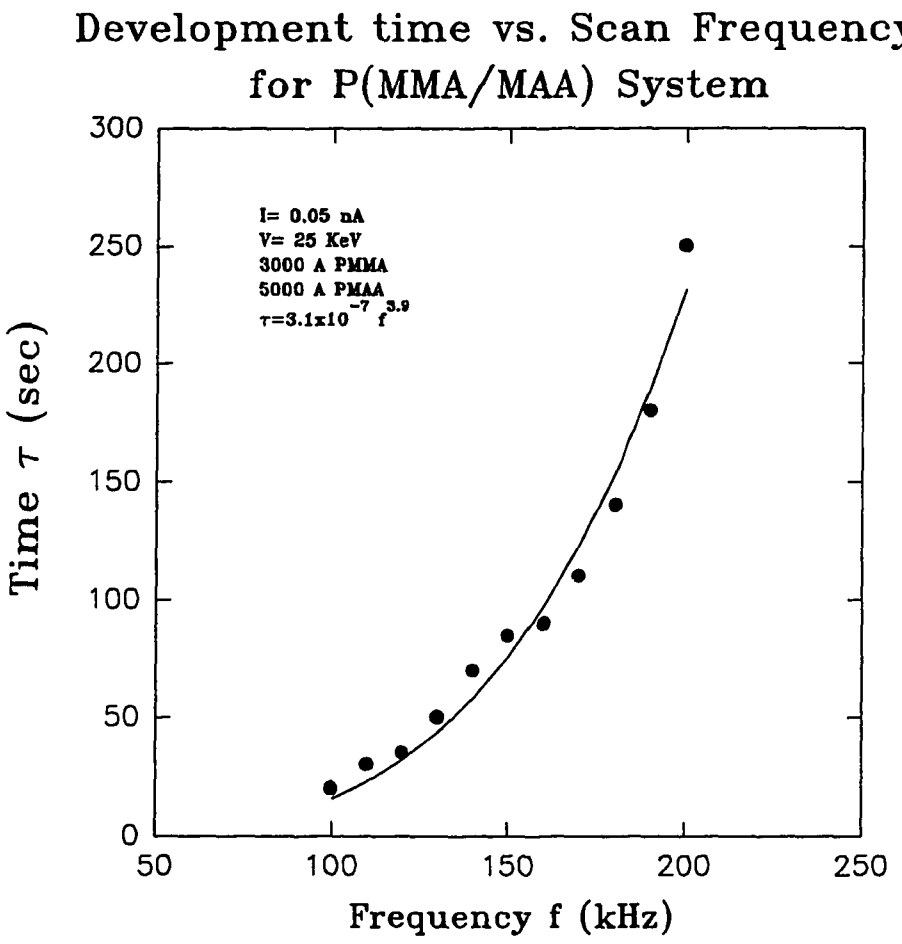

Figure 15. Development time versus scan frequency for 3000 Å PMMA atop of 5000 Å of P(MMA/MAA).

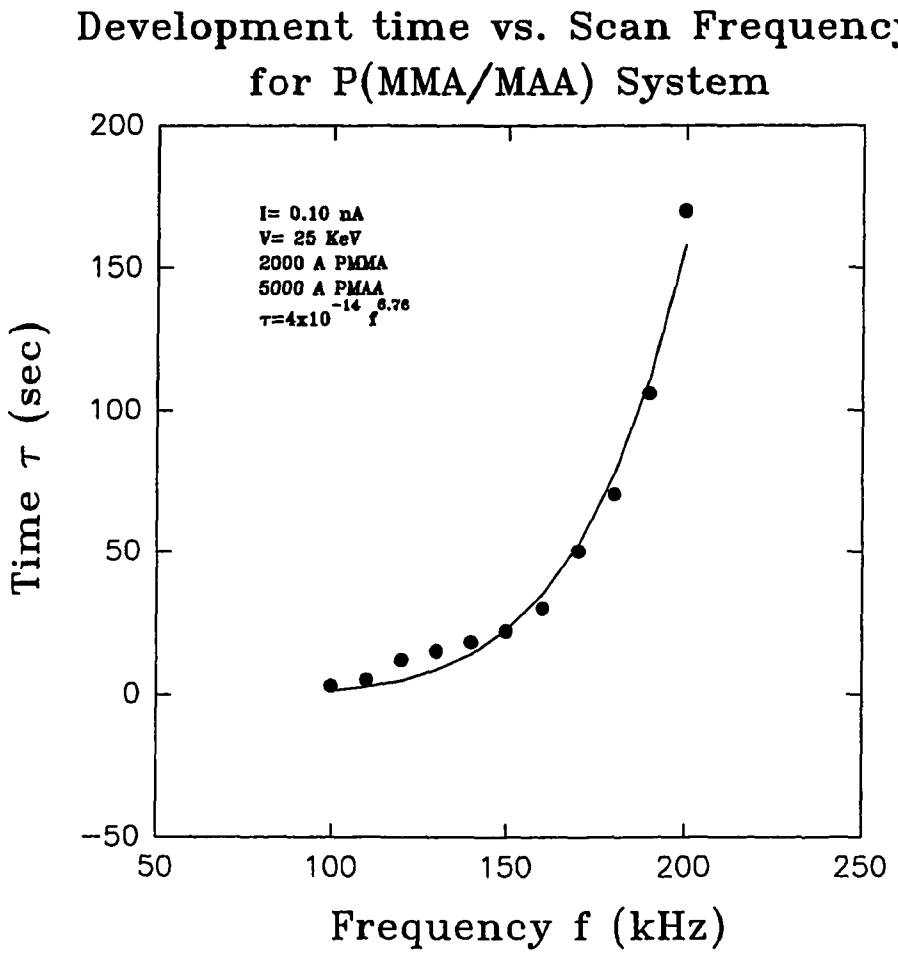

Figure 16. Development time versus scan frequency for 2000 Å PMMA atop of 5000 Å of P(MMA/MAA) at 0.1 nA beam current.

II.VI Shadow Mask Geometry

The standard geometry of the tunnel junction have always been the overlap type where two lines are patterned at 90° with respect to one another in succession, and the overlap between the lines defined the area of the junction (Figure 17a). The obvious advantage of the overlap geometry is the ease of fabrication. However, the overlap geometry suffers from excessive parasitic capacitance. Furthermore, the Coulomb blockade temperature of 1 K imposes the conditions that the junction area be no larger than 1000 Å by 1000 Å and the electron beam resolution of no greater than 250 Å, which is extremely difficult to achieve in the overlap geometry. In addition, formation of a good tunneling barrier is best achieved without breaking the vacuum, and the overlap geometry precludes that possibility.

The shadow mask geometry (Figure 17b) was developed to address the problems listed above. The shadow mask geometry basically consisted of two lines written very close to one another end to end. The spacing between the end of the lines is an undeveloped portion of the PMMA about 0.1 μm wide suspended above the substrate (Figure 17c). Two oblique angle evaporations from opposite sides of the suspended PMMA defined the junction. Since the two lines connecting the junctions area are 180° apart, the parasitic capacitance of the leads to and away from the junction is minimized. In addition, the oblique angle evaporations defining the junction can be done without breaking vacuum, thus insuring the integrity of the tunneling barrier. Furthermore, the junction area is now dependent only the angles the oblique evaporations, which is considerably easier to control, and no longer dependent upon the ultimate resolution of the microscope itself.

The tradeoffs of the shadow mask geometry are it fragility and dependence on the preparation of the bilayer P(MMA/MAA) resist and the post-exposure processing the resist.

Because the shadow mask is a free standing sub micron structure itself, and its structural integrity depends on the elasticity of the resist; the chances of the shadow mask surviving the various blow drying and baking processes of the fabrication steps are slim. The small size of the shadow mask itself makes it very process-dependent; a small variations in dosage or variations in the thickness of the resist alters the size of the shadow mask, which in term affects the overall size of the tunnel junction.

The development of the shadow mask technology used in this process was the single most difficult and time-consuming task involved in this work.

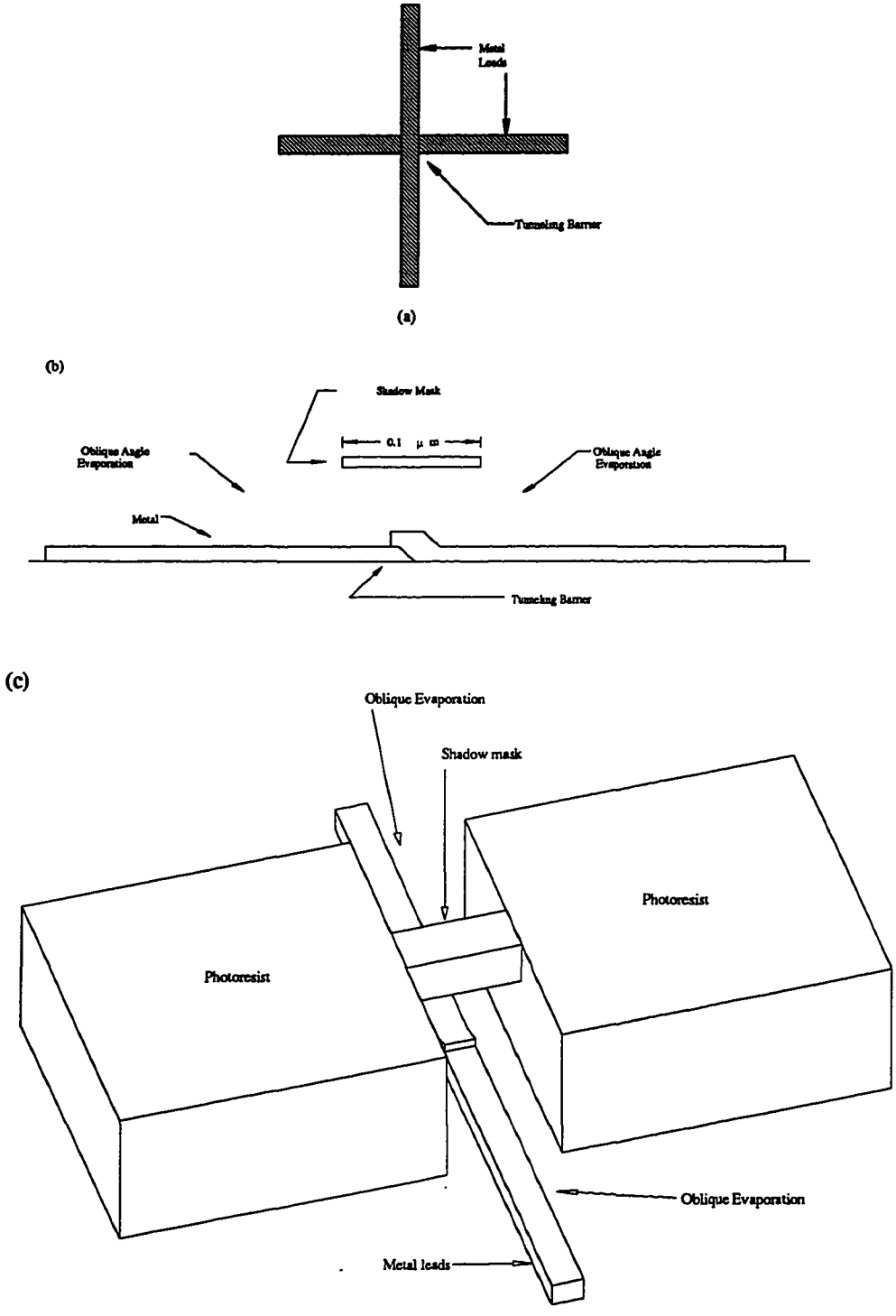

Figure 17. The overlap geometry: **(a)**.
The shadow mask geometry: **(b)** side view, **(c)** 3-D rendered.

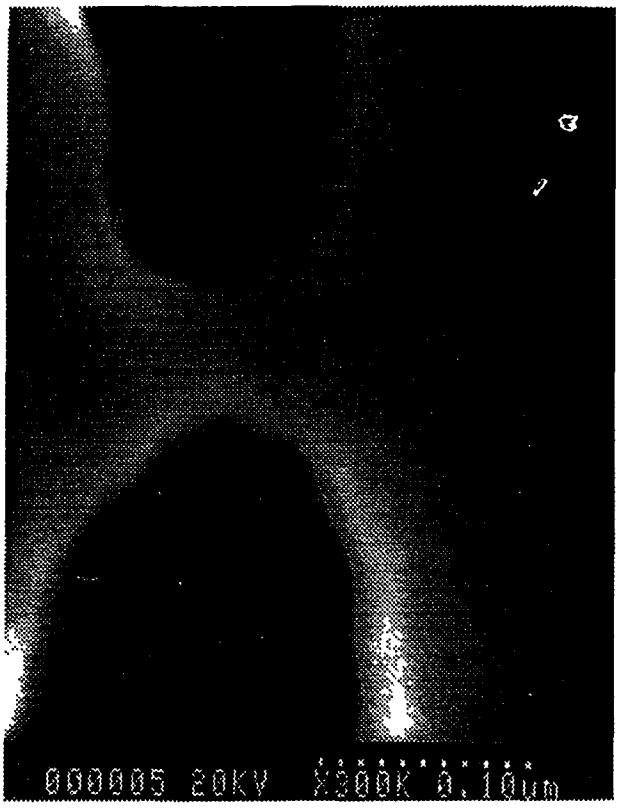

Figure 17. (d) The actual shadow mask. The width of the bridge structure was measured to be 700 Å.

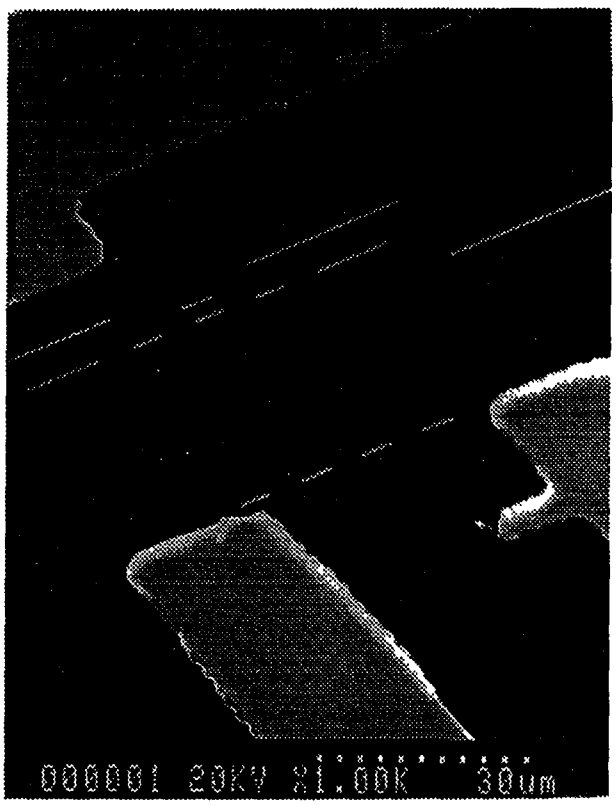

Figure 17. (e) The 16 junction linear chain.

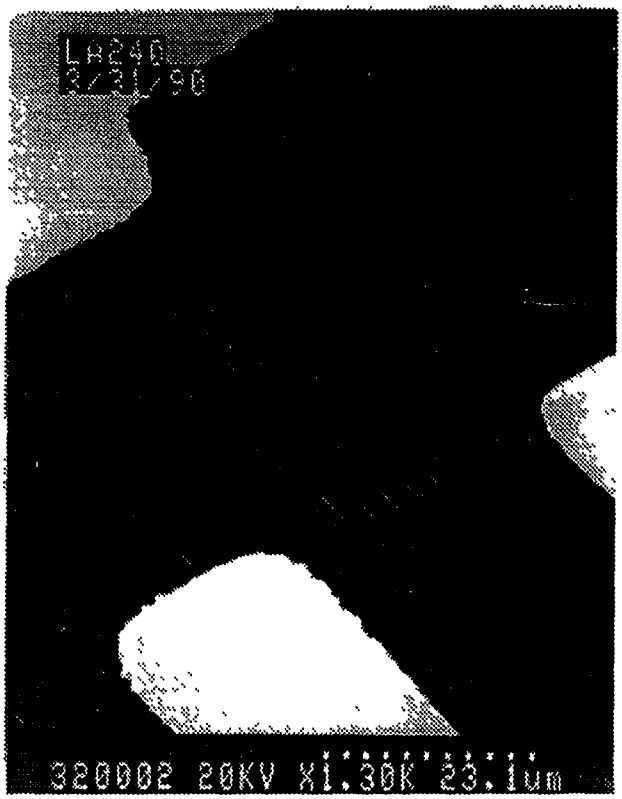

Figure 17. **(f)** The 240 junction linear chain.

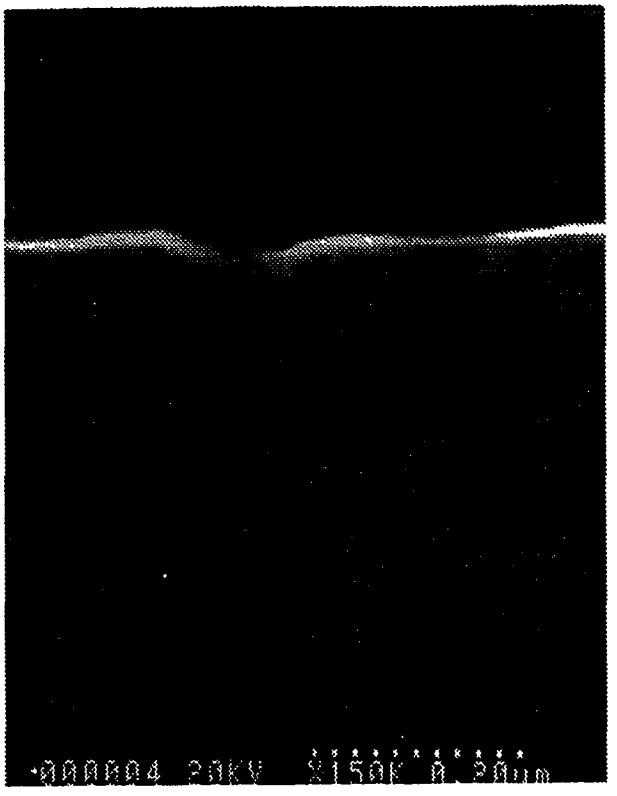

Figure 17. (g) The actual submicron Josephson tunnel junction.

II.VII Sample Fabrication

The linear junction chains studied for this work consisted of 12 and 164 junctions arranged along a serpentine line. The inter-junction spacing were 9 μm in the short chain and 2.5 μm in the longer chains. The devices were fabricated with the shadow mask technique described previously.

The electrical contact pads are prepared first. The Si substrates were cleaned and baked dried at 200º C. After allowing the substrates to cool to room temperature, the substrates were subsequently treated with HMDS[3] at room temperature for 5 minutes to passivate any remaining surface moisture. The photoresist PR-1350 were spun onto the substrates at 4000 RPM for 30 seconds. After baking the resist-coated substrates at 90º C for 30 minutes, the substrates were exposed on the Karl Suss mask aligner for 45 seconds. The exposed substrates were developed in 4:1 H_2O:PR-4011 for 30 seconds. The substrates were put into a Sputter Films sputtering systems and 1200 Å of W was sputtered onto the watered-cooled substrates at a rate of 10 Å/sec. The samples were lifted off in acetone overnight. After the lift-off, P(MMA/MAA) was first spun onto the substrates at 7000 rpm for 30 seconds, then baked at 160° C for 30 minutes. The PMMA later was spun on top of the P(MMA/MAA) at 7000 rpm at 30 seconds, and baked again at 160° C for 30 minutes.

Pattern registration was done on a modified JEOL-35C scanning electron microscope with a Tungsten source. The column optics of the microscope is checked and re-aligned before every e-beam writing session after the Tungsten source was thermal annealed.

After the pattern registration, samples are developed in 3:1 Isopropyl alcohol:2-Ethoxyethanol for 10 to 50 seconds to remove the exposed areas of the resist.

---

[3]Hexamethyldisilazane

Metallization is achieved in a Commonwealth evaporator equipped with a variable -angle water-cooled stage. Once reaching low pressures (~ 1μTorr), 350 Å of Aluminum is then evaporated onto the substrate at oblique angle (+17°). The freshly evaporated Aluminum film is subsequently exposed to dry Oxygen between 1 to 10 minutes before the last 350 Å of Aluminum is evaporated onto the substrate at oblique angle (-17°), thus completing the junction. Soaking the substrates in Acetone overnight completes the final liftoff.

As a final step in the process, metal contact pads are evaporated onto the substrates, completing the electrical contacts between the large Tungsten contact pads and the Aluminum lines.

Since the devices studied for this work were primarily low resistance devices, we have carried out extensive microstructual, chemical and electrical characterizations of the Aluminum films. The TEM studies showed the films to be polycrystalline with a nominal grain size of 125 Å. Auger and SIMS studies showed the films to be relatively free of impurities; SIMS data have placed the upper limit of impurity concentration at 100 ppb. A separate sample was prepared without any tunneling barriers in order to characterize the electrical properties of the leads. The lead resistances were found to be 100-150 Ω, resistive and insensitive to temperature variations.

The tunneling resistances and capacitances per junction for the devices studied are listed in Table 1. Although it is difficult to verify the uniformity of the junctions in the chains, the area estimates from SEM micrographs and SIMS depth profile analysis of the oxide barriers in large area tunnel junctions suggested that junctions are matched to within ±20 %. In addition, the measurements on the IV characteristics of linear chains showed sharp 2Δ rise at the superconducting gap, attesting to the uniformity of the junction chains.

Table 1. The relevant parameters of the samples measured are listed in order of decreasing tunneling resistance. The capacitance of the tunnel junction were estimated from geometric areas extracted from electron micrographs. Resistances and capacitances are single junction parameters.

Sample	Junctions	R_n (KΩ)	C (fF)	E_J/E_C
1	12	28.3	1.5	0.05
2	164	7.32	0.8	0.1
3	12	3.42	0.8	0.3
4	164	3.35	1.6	0.5
5	12	1.02	0.8	0.9
6	12	0.91	1.1	1.4
7	12	1.83	1.4	1.2

Chapter III

Experimental Setup

III.I Introduction

This chapter describes the cryostat and electronics used in the experiments.

The cryostat used for this is of the home-built single-shot type ^{3}He refrigerator consisting of a ^{3}He insert with the appropriate pumping systems. The thermometry of the system consists of a commercial Ge thermometer and two calibrated Speer resistors, a lockin amplifier, an home-built AC inductance bridge, and a home built temperature controller.. The electronics of the experimental consists of a home-built current source, appropriate commercial preamplifiers, and a computer for signal averaging.

This chapter gives a brief description of the various components used in the experiments. Figure 20 shows the overall system layout, and figure 21 shows the layout of the He^3 pot itself. The various information including calibrations and operating procedures will be discussed.

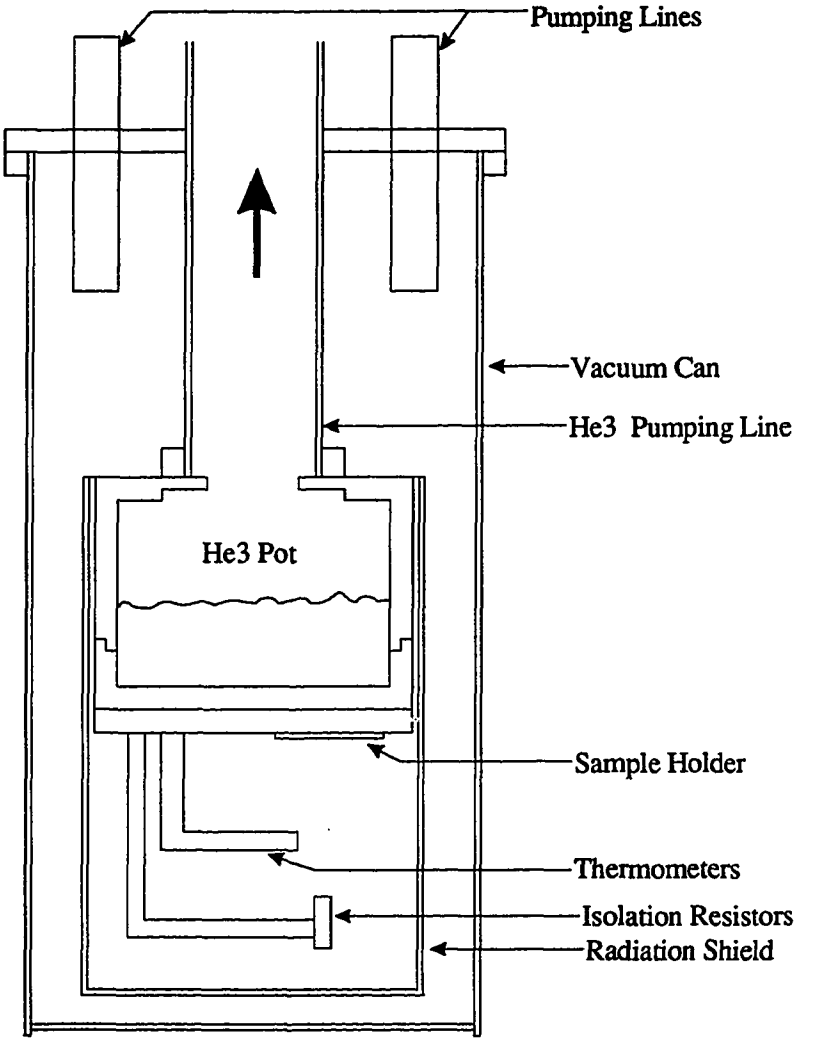

Figure 20. The ^{3}He pot.

III.II Cryostat

The cryostat used in this work consists of a super insulated dewer, a ^{3}He insert, ^{3}He pumping station, and ^{4}He pumping lines for the bath.

The ^{3}He insert used in the work is of the conventional one-shot design; it consists of a ^{3}He pot, appropriate wiring for thermometry and samples, a radiation shield, a vacuum can, and all the necessary tubing for pumping and condensation of the ^{3}He.

The ^{3}He pumping station consists of one ordinary liquid nitrogen cold trap, a larger trap filled molecular sieves, all the assorted valves and pumping lines, and diffusion pump backed by an conventional mechanical pump. The ^{4}He bath is pumped via the in-house pumping lines to a recovery system.

During normal operations of the cryostat, the super insulated dewer and the insert is precooled with liquid Nitrogen to 77 K, then liquid Nitrogen is siphoned out and liquid ^{4}He is transferred to the dewer in order to cool the insert to 4.2 K. Throughout precooling, the vacuum can outside the ^{3}He and the ^{3}He pot are pumped continuously throughout the precooling process. No exchange gas is used for precooling; this ensures precooling process to be slow and deliberate and minimizes the possibility of thermal shock to either the insert or the samples. The entire precooling process usually take about two days.

Once at 4.2 K, liquid ^{4}He is transferred again to the dewer and the bath is pumped down to 1.1 K via the in-house mechanical pumps and blowers. While the bath is slowly cooling to 1.1 K, the ^{3}He gas is route through the cold trap and molecular sieves on order to remove any condensable gases at the ^{3}He pumping station. The ^{3}He gas is then finally released into the ^{3}He pot through a small capillary tube and allow to condense slowly into the ^{3}He pot. The condensation process takes about 4 hours provided that the bath temperature remained as low as possible throughout the condensation period.

After the ^{3}He is fully condensed into the ^{3}He pot, the pot can then be pumped and cool further. At this point, the pumping line to the vacuum can is sealed off. Since no exchange gas is used, good thermal insulation between the ^{3}He pot and the ^{4}He bath is guaranteed. When pumping on the ^{3}He pot, the desired temperature of the ^{3}He pot can be dialed into the inductance bridge. When the desired temperature is reached, the temperature controller is automatically turned on to maintain the desired temperature by drive a small heater located at the bottom of the ^{3}He pot. The experiment begins once the temperature is stabilized. The average running time of the cryostat is 14 hours. The lowest temperature the cryostat can regularly reached under normal conditions is 0.4 K.

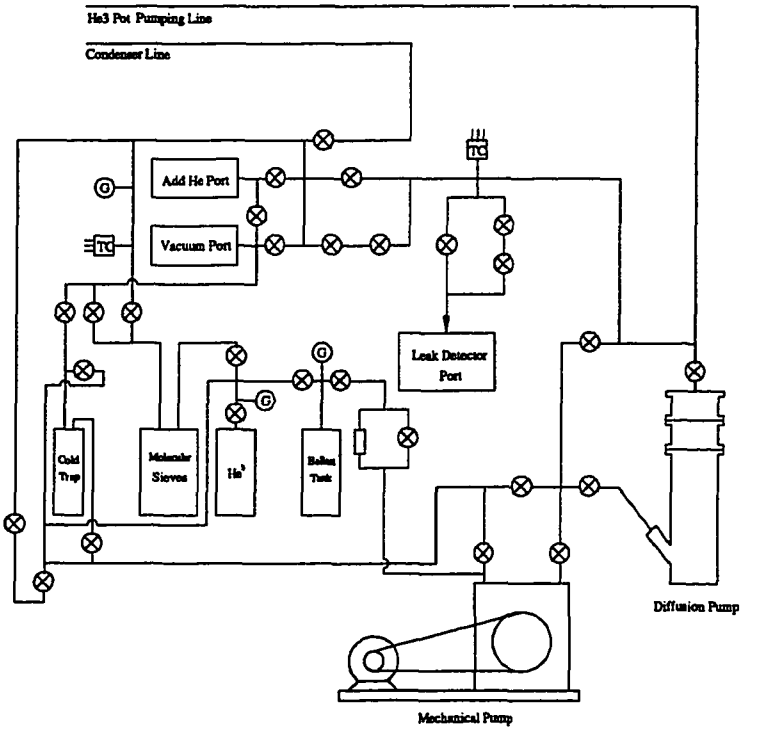

Figure 20. The He^3 pumping system.

III.III Thermometry

The thermometry of the system consists of one commercial Ge thermometer, two Speer resistors, a home-built AC inductance bridge, a PAR lockin amplifier, and a home-built temperature controller.

The Ge thermometer used in the insert was commercially calibrated down to 1.4 K, and both of the Speer resistors were calibrated down to 0.1 K against a Ge thermometer on a different system.

The schematics of the AC inductance bridge[14] is showed in figure 22, and the calibrations of the two Speer resistors are shown in figures 23 and 24.

During normal operation, the resistance of the thermometer , R_T, is related to the reference resistance, R_S, by a constant:

$$R_T = \alpha \bullet R_S \qquad \text{(III.III.1)}$$

The values of α was determined by the value of the inductance for the bridge used, and the values of the different reference resistances are summarized in the table below:

R_s , Nominal value	R_s , Measured value
100 KΩ	101.69 KΩ
10 KΩ	10.034 KΩ
1 KΩ	0.9966 KΩ

Table 2. The measured values of various reference resistors used in the inductance bridge.

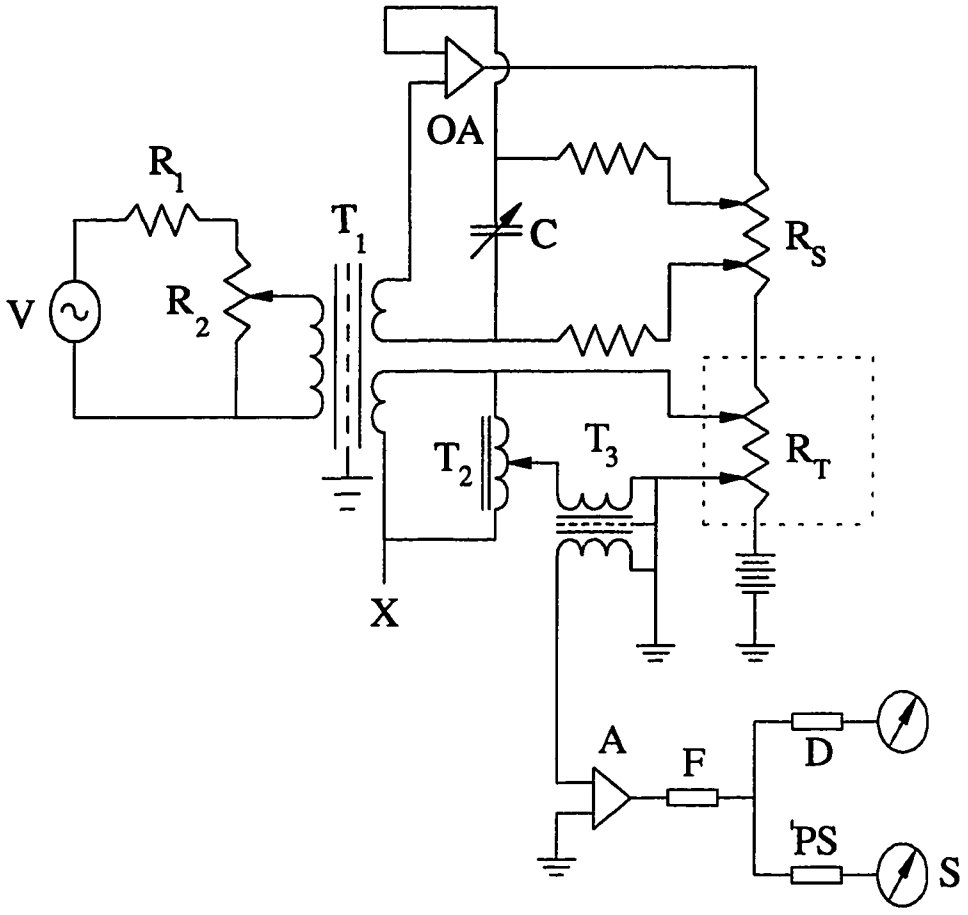

Figure 22. The schematic of the AC inductance bridge.

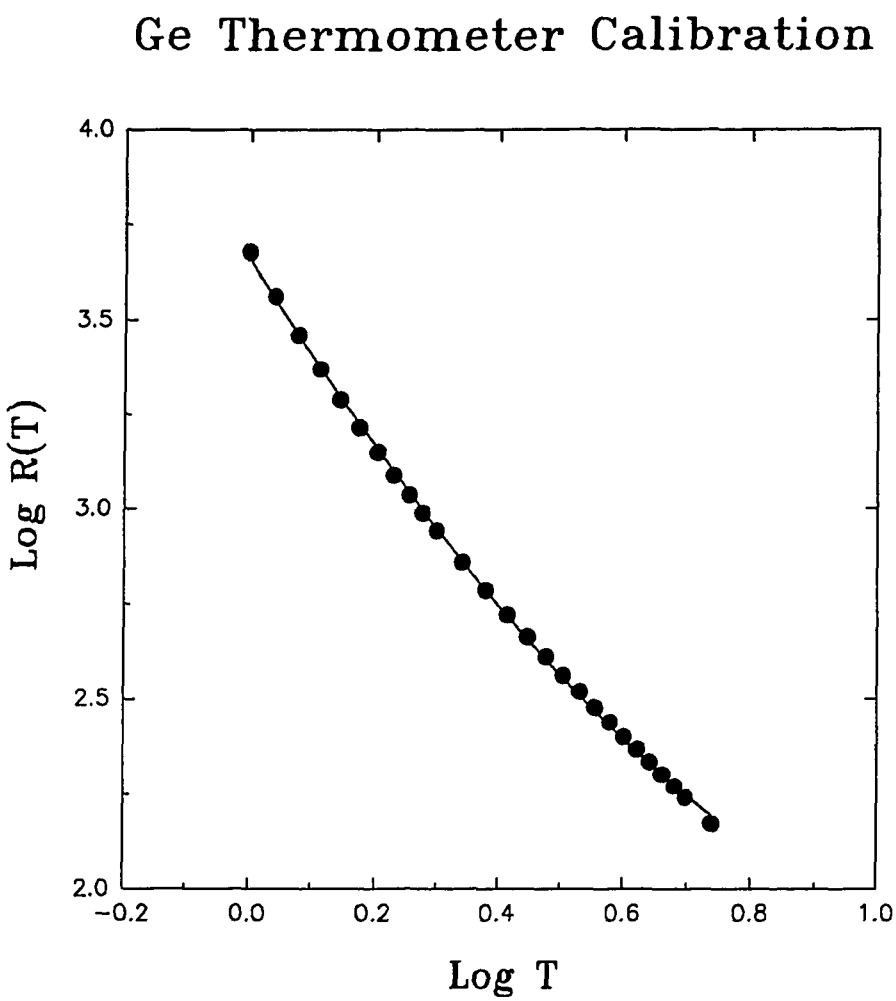

Figure 23. Germanium thermometer calibration. The data was fitted with 10th order polynomial.

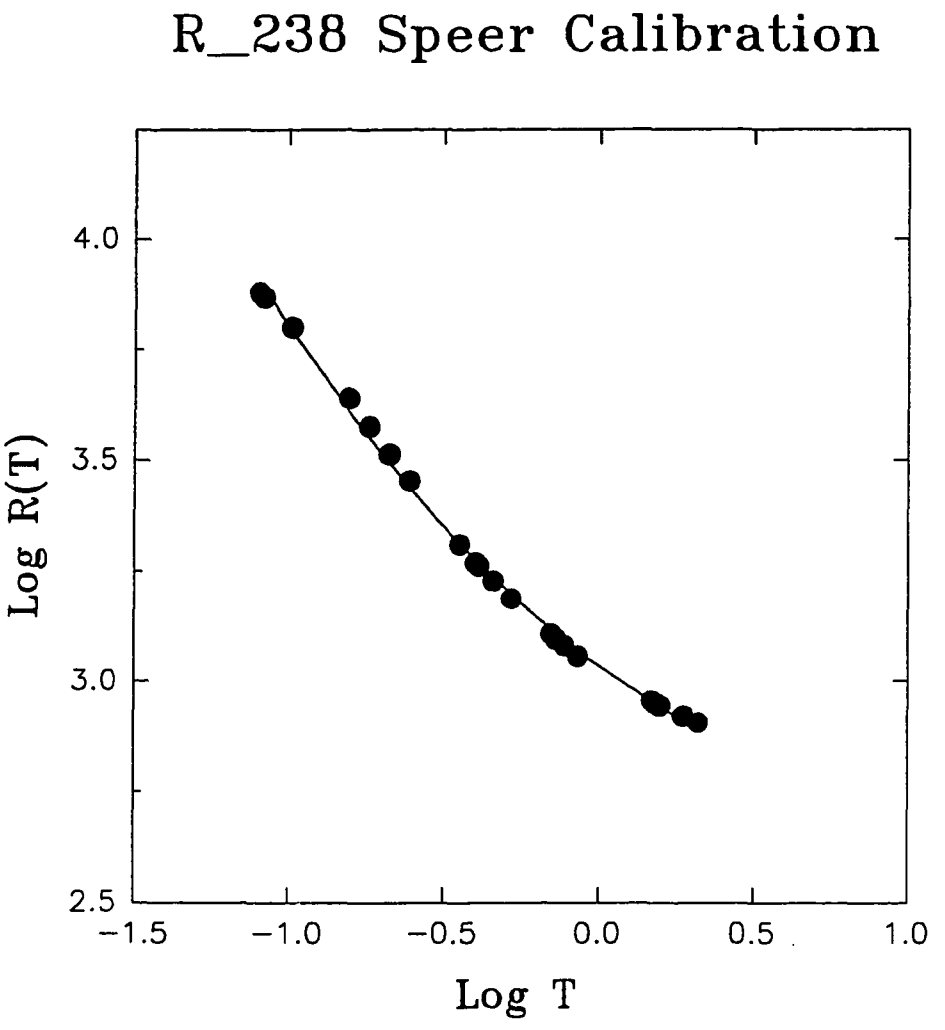

Figure 24. Speer R_238 resistor calibration.

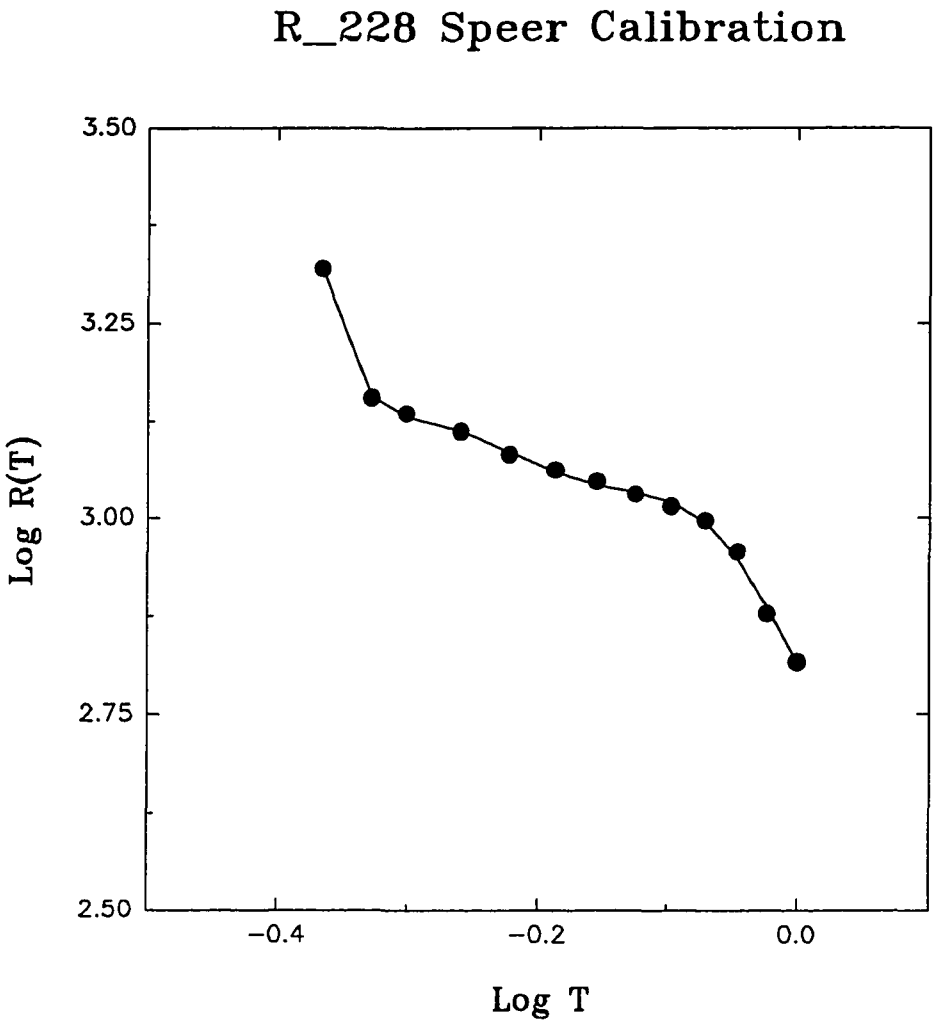

Figure 25. Speer R_228 calibration.

III.IV Measurement Setup

The IV characteristics of the devices studied were taken with a current source[4] in the usual four terminal configuration (Figure 26).

The current source puts out a current proportional to a ramping voltage generated by the computer. To measure the actual current flowing through the sample, the current was passed through a 1 MΩ resistor in series with the device and the voltage drop across the resistor was measured with an Ithaco preamplifier in the 4 terminal configuration; Ohm's law yields the value of the current. The voltage of the devices were measured in the similar manner.

High resistance alloy wires were used throughout the insert in addition to the high resistance inline resistors, the overall room temperature input impedance of the measuring circuit was at least 1 MΩ from the preamplifiers, the Thevenet equivalent of the outside noise sources, , as seen from the sample, would appear as a voltage source with an 1 MΩ output impedance.

The overall noise of the measurement setup were measured to be about 3.2×10^{-17} V^2/Hz. The noise measurement was taken with a 20 Ω metal film resistor taking the place of the sample. The Johnson noise of the 20 Ω metal film resistor was subsequently subtracted from the overall power spectrum of the experimental setup, yielding the noise figure of the experimental setup minus the sample. The noise measurements were repeated under various conditions with other sources of possible noises, such as mechanical pumps and lights turning on and off during measurements with negligible consequences. The dominant source of the noise in the experimental setup came from the commercial preamplifiers used in the experiments.

---

[4]The distinction between current biasing and voltage bias is not as important in linear chains since only the two outermost junctions are affected, and their contribution to the overall IV characteristics decreases with increasing chain length. With voltage biasing, the voltage across the entire chain is constant, but the voltages of the junctions within the chain, other than the outermost two junctions, are allowed to vary. On the other hand, current biasing allows all the junction voltages to vary as to keep the current within the chain constant. As the chain length grows, the difference between the two cases become less significant.

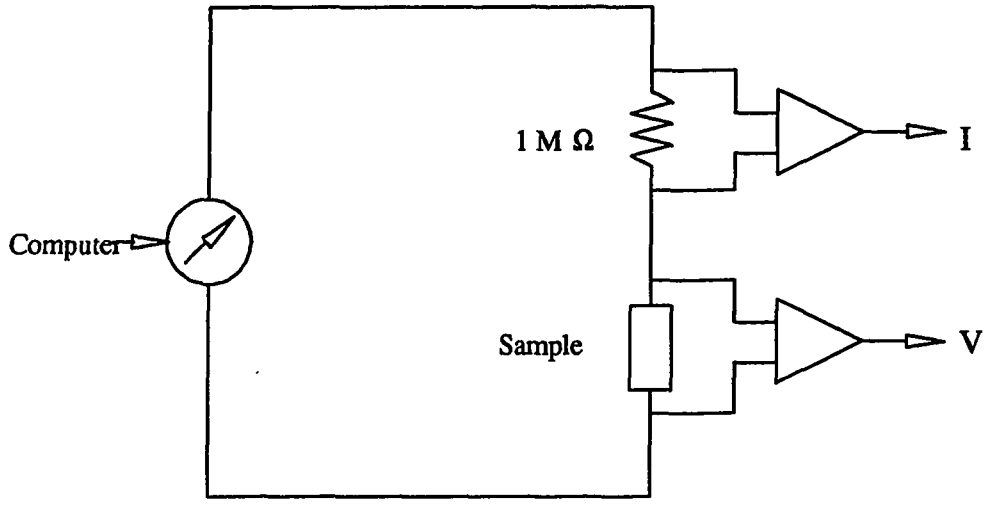

Figure 26. The standard 4 terminal configuration. The current I and voltage V are measured as the computer ramps the current source.

Chapter IV

Experimental Data

IV.I Introduction

A considerable amount of theoretical works has been published in the literature on the subject of re-entrant superconductivity since the experimental results of Goldman et. al.. While the details of the calculations vary from theory to theory, almost all of the theories have assumed the quasi-reentrant effects observed by Goldman and coworker were the direct consequence of the competition between charging and Josephson effects. Although the granular films studied by Goldman et. al. have never been fully characterized, they have always assumed the films to be discontinuous and highly disordered at the percolation threshold. The typical inter-grain capacitance of the granular films was estimated to be about 0.001 fF, making the charging energy (~ 100 K) considerably larger than any of the ordinary "low temperature" superconductors (~ 1 K). Near the superconducting transition, where the quasi reentrant superconductivity was reportedly observed, the charging energy was believed to be of the same order of magnitude as the Josephson coupling energy. Thermal fluctuations near the superconducting transition should affect both charging and Josephson effects. In addition, quasiparticle conduction near the superconducting transition should play a major role in the overall transport properties of the granular films, but it was never seriously considered in the literatures.

Looking back at the RSJ model of the Josephson junction, where a shunting resistor is connected across the ideal junction, and carrying part of the overall currents flowing through the real junction. It behooves one to ask the question: if instead of the classical ohmic shunt resistor, the resistor becomes temperature dependent and represents the quasiparticle contribution to the overall transport properties of the junction; with its activated temperature dependence, the quasiparticle conduction offers a viable alternative to charging effect as the source of competition against the Josephson effect. In fact, quasiparticles, with its temperature dependence, may replace the charging effect as the dominant effect the Josephson effects has to compete with. However, competition alone will not produce quasi-reentrant behavior; one needs disorder.

Disorder in granular films may manifest it self as a distribution of grain sizes, geometry, inter-grain capacitance or Josephson coupling energy. At the percolation threshold, a slight distribution in inter-grain Josephson coupling energies lend credence to the idea that one and only one conduction path is possible across the disordered granular film.

Therefore, the goal of the experiment is to model the behavior of the granular system at the onset of conduction with linear chain of Josephson tunnel junctions in relatively low resistance devices and to study the properties of the chains as functions of their normal state resistances and temperature in order to elucidate the origin of the quasi-reentrant behavior.

Because of the high frequency of the Bloch oscillations, there were some experimental evidences on the effects of local electrical environment on the IV characteristics of the devices undergoing Bloch oscillations. The electrical environment manifests itself through the parasitic capacitance C and inductance L of the electrical leads connecting the devices to the outside world. For a device connected to the outside world with low resistance leads, the electrical environment smears Coulomb gap by introducing fluctuations of the order $2\pi\hbar/\sqrt{LC}$.

In order to account for the effects of electrical environment on the IV characteristics of the chains, we have fabricated chains with two different lengths with different inter-junction separations to account different inductances and varied the inline isolation resistors to account for effects by the parasitic capacitances of the systems. No significant changes in the IV characteristics were ever observed over all temperature ranges. The effects of electrical environment on the IV characteristics were probably minimal at best.

Although the electrical environment did not play an important part in the smearing of the Coulomb gap, the resistance of the junction chains did. Figure 31 shows the dynamic resistance of the junction chains at different junction resistances. The peaks of the dynamic resistances decreases with decreasing junction resistance. The height and width of the peaks do not agree with the theoretical prediction of Licharev et. al.. In addition, the maximum increase in the resistance at zero bias amounted to at most 50% of the junction resistance in the devices with $E_J/E_C \approx 1$ at the lowest temperatures. Comparing to the results of Goldman et. al., where the increase often approaches ∞ at the lowest temperatures, suggests that charging effect may not have played as important a role in the transport properties in the linear chains and granular films as suggested by others. The disapperaance of the Coulomb blockade in the 0.95 KΩ device was the result of dissipation, and it can be understood in terms of the uncertainty principle:

$$\Delta E \cdot \Delta t \geq \hbar/2 \qquad \text{(IV.I)}$$

With $\Delta E = e^2/2C$ and $\Delta t \approx RC$, the uncertainty expression gives the lower bound on the resistance of $\hbar/e^2 \approx 3.2K\Omega$ below which no Coulomb blockade can exist. The apparent discrepancy between the expected value of 3.2 KΩ and the observed value of .95 KΩ may be due to the large uncertainty in the capacitance and the local parasitic capacitance of the junctions.

The noise measurements on the systems and preamplifiers showed that the noise floor of the system at 3.2 x 10^{-17} V^2/Hz. The bandwidth of the data during the voltage

ramp was approximately 1 Hz, giving a noise voltage of approximately 4×10^{-9} volts. Comparing to the IR values of the 0.95 KΩ device in figure 32, which were 3 orders of magnitudes larger than the noise voltage, we concluded that the disappearance of the Coulomb blockade could not be due to external noise sources.

However, the electrical leads do more than just smears the Coulomb gap. Quasiparticles often exhibit long range coherence within long electrical leads. This effect is purely the consequence of the presence of the superconducting parameter and the phase coherence of the superconducting ground state.

In many instances, quasiparticles behave much like normal electrons. However, normal electrons do not exhibit the long range coherence of the quasiparticles. The effects of long range quasiparticle coherence become significant in long electrical leads, such as the ones connecting the ultra small tunnel junctions to the electrical contact pads in the devices studied. The long range coherence of the quasiparticles manifest themselves as discrete steps in the IV characteristics of the Josephson junctions.

Another aspect of the data is the appearance of the dynamic resistance oscillations. Such oscillations have also been observed by the author in linear chains. The oscillations may be cause by either the presence of charge traps or by presence of extreme coupling energy disorder amongst the junctions within the chain.

IV.II Temperature Dependence

Figure 4 shows the typical IV characteristics of a linear chain of ultra small normal tunnel junctions. The IV characteristics showed the typical voltage offsets indicating Coulomb blockade.

Figure 27 shows the IV characteristics of a linear chain of ultra small Josephson tunnel junctions. The major features of the IV characteristics are:

1. The slope of the supercurrent branch, which is the dynamic conductance, is no longer infinite, but has a finite slope; the finite slope suggests that the Josephson junctions are thermally excited out of the washboard potential well, and phase slips across the junctions are always non-zero.
2. The low temperature Josephson junction chain IV characteristics show a distinct voltage offsets at large biases superimposing on top of the otherwise usual Josephson IV characteristics, indicating presence of Coulomb blockade in these devices.
3. The extremely sharp 2Δ rise in the IV characteristics of the low resistance devices indicate the quality of the tunneling barriers.

Dynamic resistance studies of the junctions in their normal state showed that charging effects were not significant near the superconducting transition temperature of the films. Even in the highest resistance devices, the maximum change in the resistance believed to be due to charging amounts to be about 10% of their normal state resistances. Comparing to the temperature dependence data of the chains (figure 29), where the resistance of the devices increases exponentially with decreasing temperatures, it did not seemed possible that charging effects was the cause of the exponential increase in resistance at low temperatures.

Some of the other major features of figure 29 are summarized below:

1. The dynamic resistance increases with decreasing temperature for devices with high junction resistance.
2. The dynamic resistance decreases with decreasing temperature for devices with low junction resistances.
3. The oscillations of the dynamic resistance as function of temperature may be caused by the presence of charge traps modulating the junction resistances.

As it was mentioned before, the most important aspects of the linear chains is its controllability and geometry. The controllability of the chains allows one to change the resistance of the device in a predictable way, and to a lesser extent, the capacitance of the device as well. The geometry of the device is believed to model the behavior of the granular film at the percolation threshold. The penalty of controllability is the increase of the characteristic capacitance of the device; this effectively moves the charging energy to about 1 K and below.

The important point of the experiment data on the linear chains is that the temperature dependence of the zero bias resistance of the linear chains have reproduced the major experimental features of the granular film data.

The work of Likharev et. al. [21] considered a case of *nondissipative* normal tunnel junction suggested a function of the following form for the dynamic resistance:

$$R_d = a/\sqrt{I} \qquad \text{(IV.II.I)}$$

Where a is a constant, and I is the biasing current. The equation above suggests that increase in the dynamic resistances becomes infinite at zero bias. However, as soon as dissipation is introduced, the size of the resistance increase is substantially reduced; in addition, the width of the peaks begins to broaden as junction resistance is decreased (Figure 31). In fact, it is clear from the magnitudes of the peaks that the relative increase in the dynamic resistances never exceeded 3 to 4 times of the normal resistances even in the largest resistance devices.

The most important of feature of the data of Goldman et. al. is the quasi-reentrant behavior, and it occurred in low resistance samples where the charging energy was expected to be of the order of magnitude of the Josephson coupling energy; from the measurement of the dynamic resistance of the linear chains in their normal state, we found that the relative increase in the dynamic resistance amounts to no more than 50% of the normal state resistances in devices with $E_J/E_C \approx 1$. In addition, the temperature dependence of the dynamic resistance of the chains in their normal states showed that dynamic resistances changed very little below 1 K, and the size and width of the peaks are determined by junction dissipation alone. Taking this result at heart and compare the result of the resistance increase in the granular film data of Goldman et. al. and the dynamic resistances of the chains at zero bias (Figure 30), where the resistances of the films tend to approach infinity even for samples not very far away from their crossover resistance of the 6.4 KΩ; it is clear that relative increase in resistances at the lowest temperatures in either the granular films and chains were simply too large to be accounted for from the charging effect alone. More importantly, the quasi-reentrant behaviors observed in the granular films of Goldman et. al. occurred not in very high resistance samples at low temperatures, but in relatively low resistance samples near the superconducting transition temperatures of the films under question, where quasiparticle conduction and dissipation could be extremely important in determining the overall transport properties of the films.

The idea that quasiparticle and superconducting channels alone without charging effects in tunnel junctions may reproduce the results of granular film systems may seem odd at first, but not unexpected.

As one can recall, the quasi-reentrant behavior of the granular films of Goldman et. al. was attributed to competition between two conduction channels with opposite temperature dependences. The supercurrent has the usual tanh (Δ/kT) temperature dependence, and the Coulomb blockade has the usual exp (-δ/kT) temperature dependence. The Δ and δ are the superconducting and Coulomb gap of the junction ,

respectively. Comparing to the quasiparticle conductance of the junction, which also has the similar activated form except that the gap is the superconducting gap instead of the Coulomb gap. In fact, all that is required to have quasi-reentrant behavior is the presence of two competing conduction channels with opposite temperature dependence. Since the quasi-entrant behaviors of the granular films were observed at or near the superconducting transition also, quasiparticle conduction can be expected to be just as important as in the linear chains. The data on the linear chains indicated that charging effect is needed to reproduce most of the major features of the quasi-reentrance; all that was needed was the quasiparticles with similar activated temperature dependence. To investigate this possibility further, as very simple phenomenological model of junction conduction was introduced by the author.

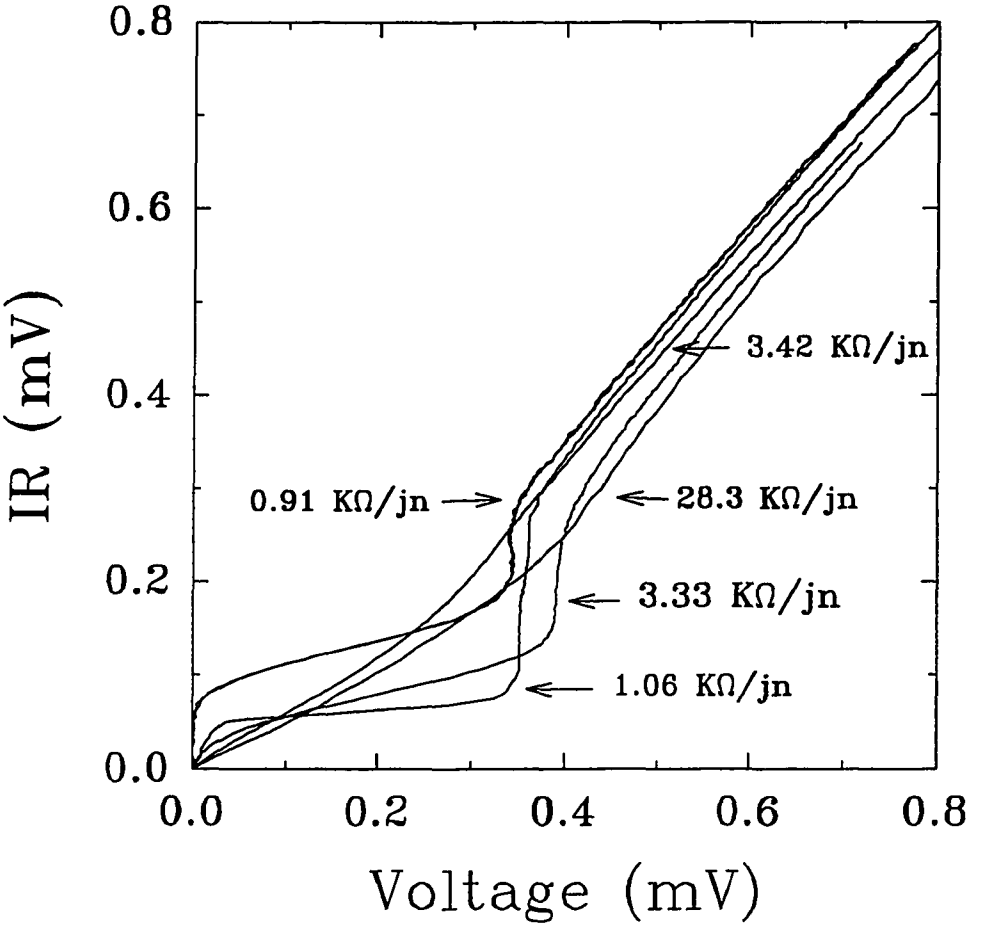

Figure 27. The IV characteristics of linear chains with different normal state resistances. The IV characteristics are normalized to per junction basis. The voltage offsets at large biases are most prominent in large resistance devices.

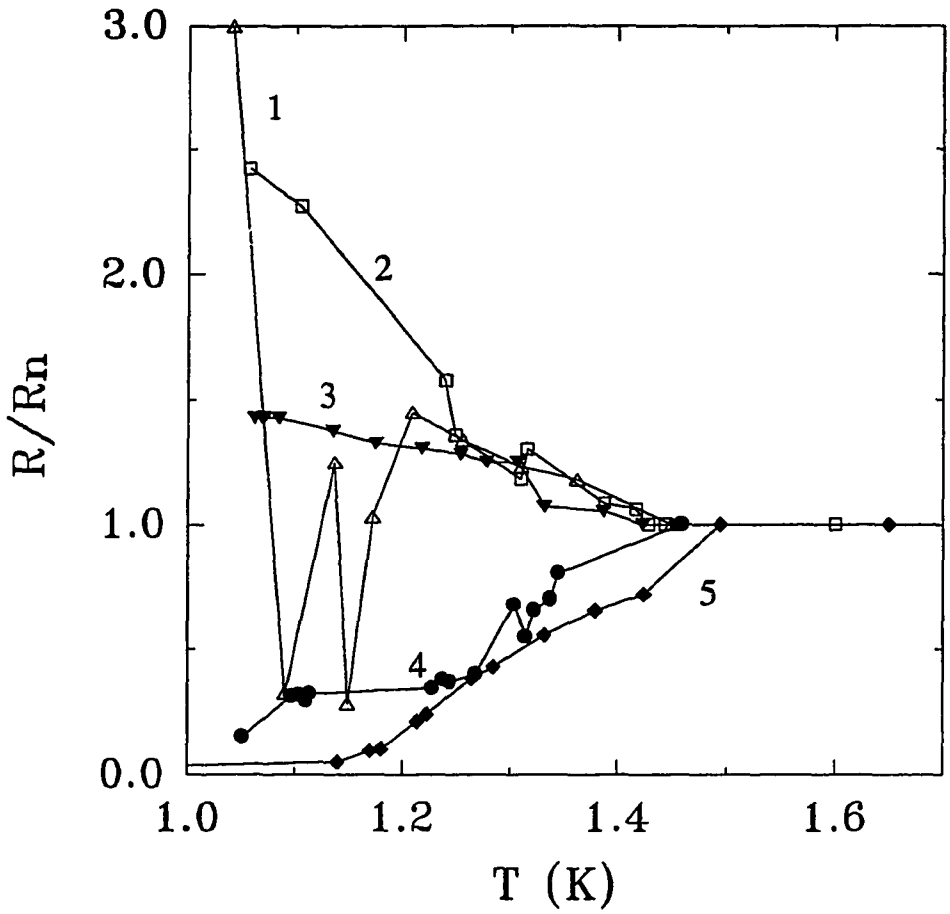

Figure 29. The temperature dependence of zero bias dynamic resistance for linear chains with various normal state resistances. The chain resistances are: **1.** 3.3 KΩ, **2.** 28.4 KΩ, **3.** 7.3 KΩ, **4.** 1.83 KΩ, **5.** 1.05 KΩ. All of the resistances are normalized to per junction basis.

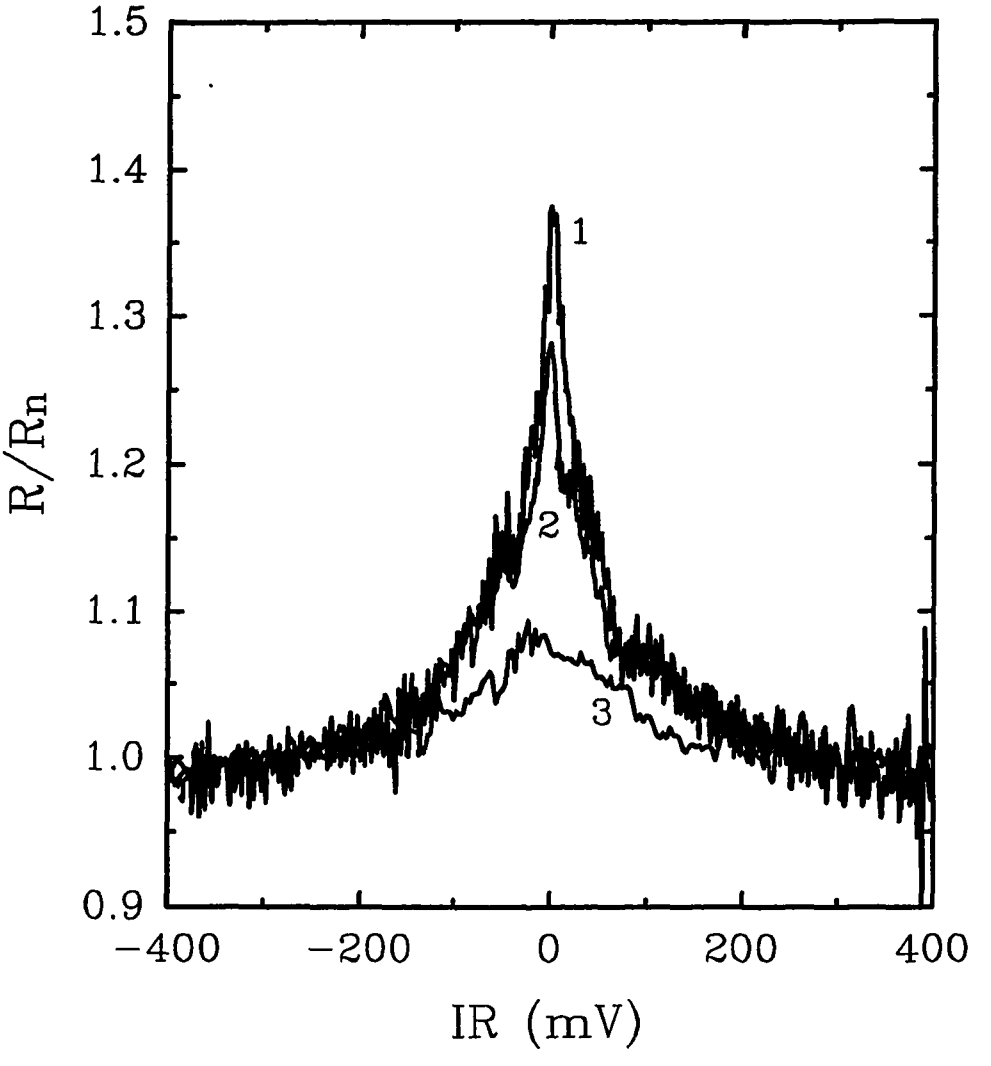

Figure 30. The dynamic resistances of a 164 junction chain at **1.** 1.07 K, **2.** 1.4 K, **3.** ~ 1.8 K. The device has a normal state resistance of 3.3 K Ω /junction. The peak due to the Coulomb blockade became temperature independent below 1.4 K, and the relative increase in resistance at zero bias is at most 50% of the normal state resistance.

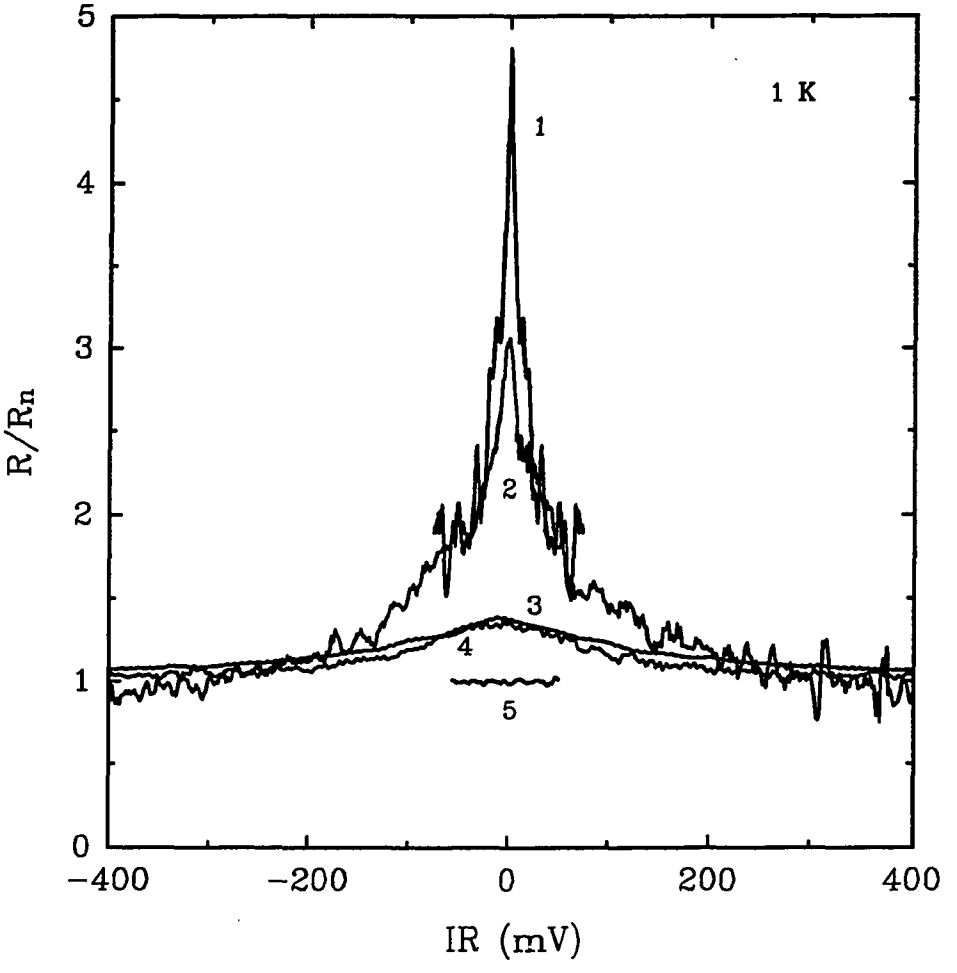

Figure 31. The dynamic resistances of junction chains with various normal state resistances. **1.** 28.3 KΩ/junction , **2.** 7.3 KΩ/junction , **3.** 3.4 KΩ /junction , **4.** 3.3 KΩ/junction, **5.** 0.95 KΩ/junction. The apparent disappearance of Coulomb blockade in 0.95 KΩ/junction device was the result of dissipation.

IV.III Zero Bias Model

The transition from quasiparticle-like to Josephson-like IV characteristics of the linear chains with decreasing junction resistances strongly suggest that the conduction in these small Josephson junctions are carried by both quasiparticles and the Coopers pairs. The simplest and the most transparent conduction model for the junction is just to treat the two conduction channels as parallel temperature-dependent resistors. At zero bias, the dynamic resistance R_D of a single junction is given as follows:

$$R_D(T) = 1\Big/\left(e^{\frac{\Delta(T)}{kT}} + \frac{\alpha}{2\pi}\int_0^{2\pi} I_0\left(\gamma \sin\left(\frac{\phi}{2}\right)\right) d\phi \right) \qquad \text{(IV.III.1)}$$

and γ is defined as

$$\gamma = \frac{\hbar\pi}{e^2 kT}\frac{\Delta(T)}{R_n}\tanh\left(\frac{\Delta(T)}{2kT}\right) \qquad \text{(IV.III.2)}$$

and R_n the normal state resistance of a single junction. The function I_0 is the zeroth order Bessel function of imaginary argument.

The exponential term represents the quasiparticle contribution to the total dynamic resistance . Likewise, the integral term represents the supercurrent contribution. With the exception of the constant α and T_C of the film, there are no other adjustable parameters in the expression. The value α can be interpreted as a weighing factor for the quasiparticle conduction channel, and it was chosen so as to reproduce the experimentally observed crossover resistance of 3.3 KΩ. The T_C of the granular Al film was measured to be 1.5 K. The superconducting gap $\Delta(T)$ has the usual BCS temperature dependence, and the rest of the symbols have their usual meanings.

To calculate the resistance of the chains, one simply compute the sum the resistances calculated via equation (IV.III.1). The presence of a narrow distribution of Josephson coupling energies causes a similar spread in both the resistance and transition temperature of the junctions. As a result, different junctions become superconducting at slightly different temperatures, giving rise to the well known quasi-reentrant behavior.

Figure 32 shows the result of computer simulation of the model. The resistances have been normalized to single junction basis by dividing the total resistance of the chain by the number of the junctions in the chain. All the major features were reproduced with this simple model, including the re-entrant behavior; all that was required to reproduce the re-entrance was a disorder in the Josephson coupling energies amongst the junctions making up the chains. The apparent oscillations in the superconducting transition temperature can not be reproduced from the model. The oscillations may be caused by the presence of charge traps within the tunneling barriers.

Considering the results of Figure 32, and if one takes the theoretical picture of Fisher et. al. one step further to the case of the linear chains near the percolation threshold, the following picture of the onset of global phase coherence of the linear chains begin to emerge: as the temperature of the system decreases, the individual Josephson junction making up the chain becomes superconducting. Because of the coupling energy disorder, each junction becomes superconducting at slight different temperatures. As a result, neighboring junctions with larger coupling energies coalesces into pockets of superconducting islands separated by junctions with the least coupling energies along the chain. As the temperature continues to decrease, the junctions with the least coupling energies eventually become superconducting, rendering the entire chain superconducting.

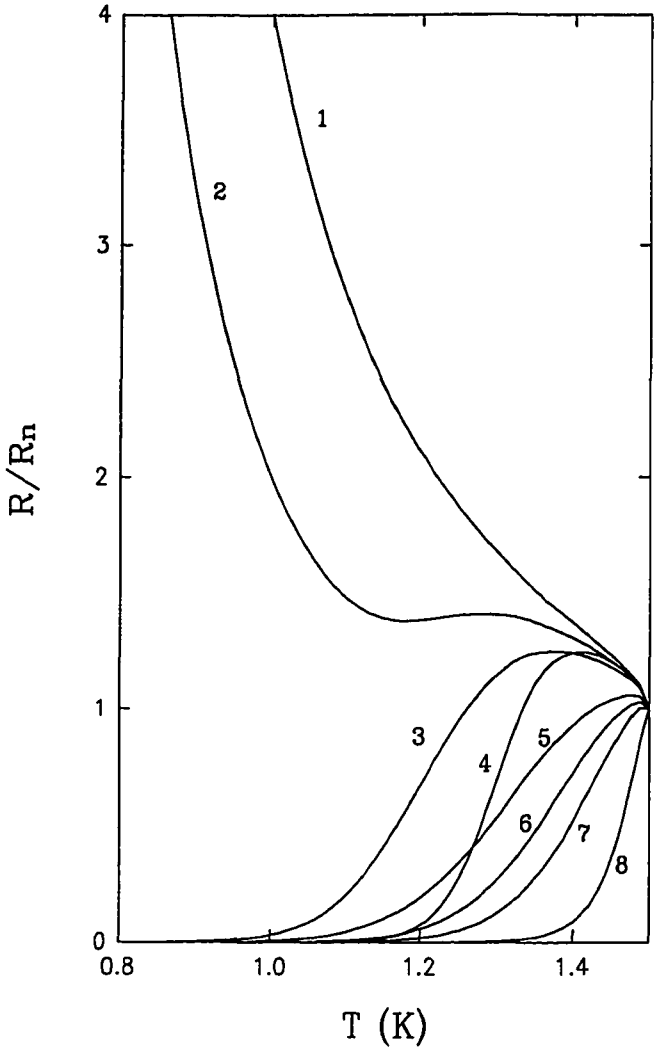

Figure 32. The temperature dependence of dynamic resistance of a linear chains with just two of the junctions within the chain with a slight deviation in the Josephson coupling energy from the norm. The re-entrant effects are the results of competition between quasiparticle and Josephson conduction within the junctions. The device resistances are: **1** 26 KΩ, **2** 1.9KΩ and 40 KΩ, **3** 1.905 KΩ and 1 KΩ, **4** 1.9 KΩ and 19KΩ, **5** 1.7 KΩ, **6** 1.5 KΩ and 2.5 KΩ, **7** 1.3 KΩ, **8** 1 KΩ.

IV.IV Dynamic Resistance Oscillations

Figure 29 shows the experimental data of linear chains that exhibited temperature oscillations. The exact source of the oscillations is not understood. However, two possibilities exist:

1. The oscillations are believed to be caused by the presence of charge traps within the tunneling barriers, thus modulating the dynamic resistance of the tunnel junction as the traps captures and release electrons. The presence of the traps have been observed in devices studied. A typical time trace of the voltage across the length of the linear chain at constant current bias showed some evidence of telegraph noise, suggesting the presence of traps within the tunneling barriers (Figure 33). In addition, the size of the junctions studied precluded the possibility of any quantum size effects. The charge traps modulates the dynamic resistance of the tunnel junctions as electrons hops in and out of the traps, giving the appearance of oscillations in the dynamic resistance.

2. The chain is highly disordered in the sense that junction resistances vary greatly from junction to junction within the chain. As a result, the junction become superconducting over a much wider temperature range than usual. Each of the dips in the resistances indicates a junction becoming superconducting as temperature was lowered.

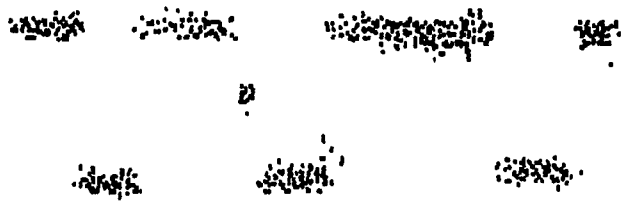

Figure 33. The time trace of voltage fluctuations of a 12 junction chain at 2 μA current bias. The trace was taken at 0.4 K. The trace was taken over 1 hour, and the magnitude of the trap noise was estimated to be about 1 mV.

IV.V Quasiparticle Coherence

Quasiparticle tunneling in these ultra small tunnel junctions have always been assumed to behave very much like normal electrons. The assumption is valid only when the long range quasiparticle coherence can be neglected, and the energy spectrum of quasiparticles can be approximated by the dispersion of normal electrons; the assumption is true only for quasiparticle states away from the gap. Near the gap, the quasiparticles can have both electron-like and hole-like properties, with four-fold degeneracy's of the quasiparticle states near the gap, long range coherence of the quasiparticles states results. If the devices studied are connected by long electrical leads made of superconducting materials, the effects of long range quasiparticle coherence can be quite significant[5]. Figure 31 is a rather spectacular demonstration of the influence of the long range coherence of the quasiparticles on the IV characteristics; the IV characteristic was from a single solitary sub micron Josephson tunnel junction connected by long superconducting leads.

The appearance of the steps in the IV characteristic may, at first, give the impression to the uninitiated as the Coulomb Staircase predicted by Mullen[12] et. al. However, a quick calculation base on the size of the voltage step yield an effective capacitance of the device three orders of magnitudes smaller than the capacitance of the device under question. In addition, the staircase pattern in figure 34 is superimposed on top of the otherwise normal superconducting IV characteristics of the RSJ Josephson junction, where the overall dynamic resistance decreases with decreasing temperature. Had the staircase the result of charging, the overall dynamic resistance should increase as temperature decreases.

In 1965, Tomasch et. al. [13] reported observing some unusual geometric resonances in the IV characteristics of thick Pb and In films; these resonance steps were

[5]A long wire can be considered as a thick film laying on its side.

shown experimentally to be related to the thickness of the film by the following empirical expression:

$$V-\Delta \approx n\left(\frac{\pi\hbar v_F}{d}\right) \qquad \text{(IV.V.1)}$$

Where $v \approx v_f$, the Fermi velocity, and Δ is the energy gap of the superconductor (Figure 36).

Shortly afterward, McMillan and Anderson suggested that these resonances were the results of long range quasiparticle interference of the electron-like and hole-like aspect of the quasiparticle states; they suggested the expression of the form:

$$|k_1 - k_2| = \frac{2\pi}{nd} = \frac{2(V^2-\Delta^2)^{1/2}}{\hbar v_F} \qquad \text{(IV.V.2)}$$

Where k_1 and k_2 are the electron-like and hole-like k vectors of the quasiparticles. Equation (III.V.2) looks remarkably similar to equation (III.V.1).

Although the details of the McMillan's theory appeared rather complex, the physics of the problem turned out to be deceptively simple.

The BCS energy spectrum of the quasiparticles have the following form:

$$E^2 = (\varepsilon_k - \varepsilon_F)^2 + \Delta^2 \qquad \text{(IV.V.3)}$$

At any particular quasiparticle energy E, there are two degenerate states corresponding to electron-like and hole-like states. The k vectors of these two states are given by the following expression:

$$k_{1,2} = k_F \pm \left(E^2-\Delta^2\right)^{1/2}/\hbar v_F \qquad \text{(IV.V.4)}$$

Each of the k vectors can be either positive or negative. Therefore, there are four degenerate states for every quasiparticle energy E near the superconducting gap; the four values of the k vectors give four plane wave solutions of the form $\exp(\mp ikx)$. The superposition of the four plane wave solutions give rise to standing wave solution of the form:

$$\psi \propto \sin(|k_1 + k_2|x)\sin(|k_1 - k_2|x) \qquad \text{(IV.V.5)}$$

If the length of the electrical lead is d, then the $|k_1 - k_2|$ will have to take on the value of 2π/nd. By using the expression of quasiparticle energy E, $|k_1 - k_2|$ can be rewritten in terms of energy gap, and we immediately arrived at the result of McMillan and Anderson (Eq. III.V.2). Figure 35 shows the graphical solution of the problem.

The long range coherence of the quasiparticles is the direct consequence of the multi-valueness of the energy dispersion relation of the quasiparticles near the superconducting gap; normal electrons with standard single-valued k^2 energy dispersion, does not exhibit long range coherence.

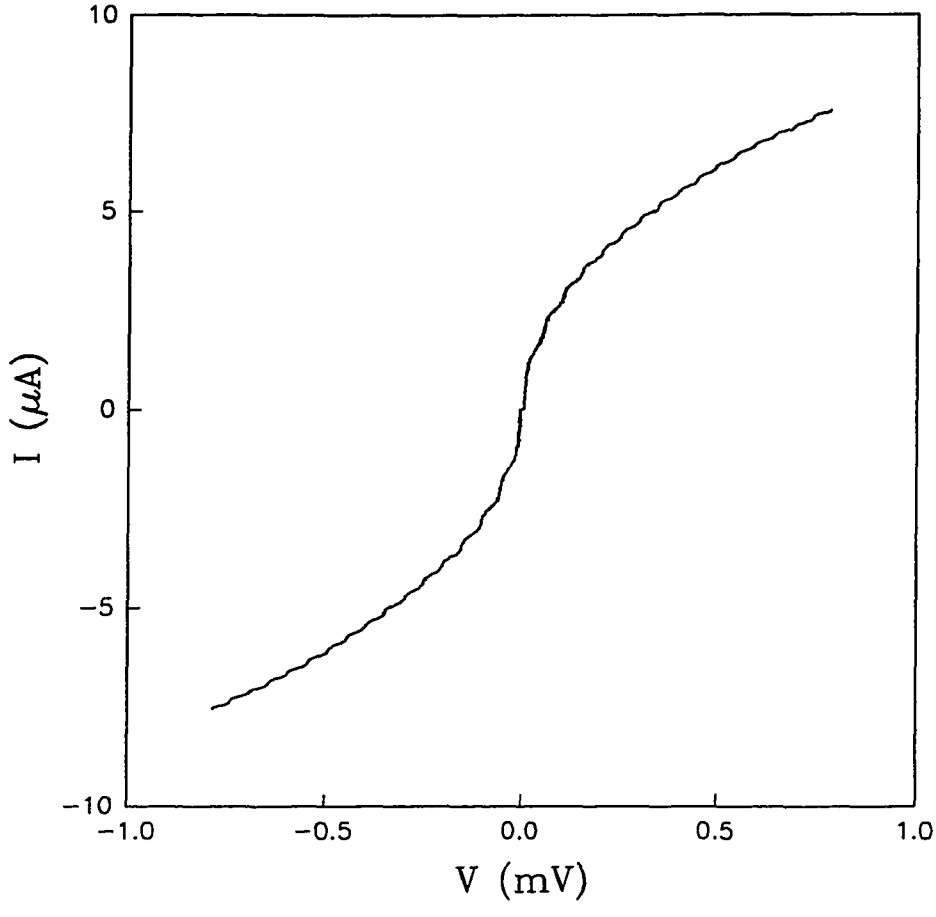

Figure 34. The IV characteristic of a solitary Josephson tunnel junction connected by two long conducting leads. The staircase pattern superimposed on top of the RSJ-like IV characteristics is the result of long range coherence of the quasiparticle states. The IV characteristic was taken at 1 K.

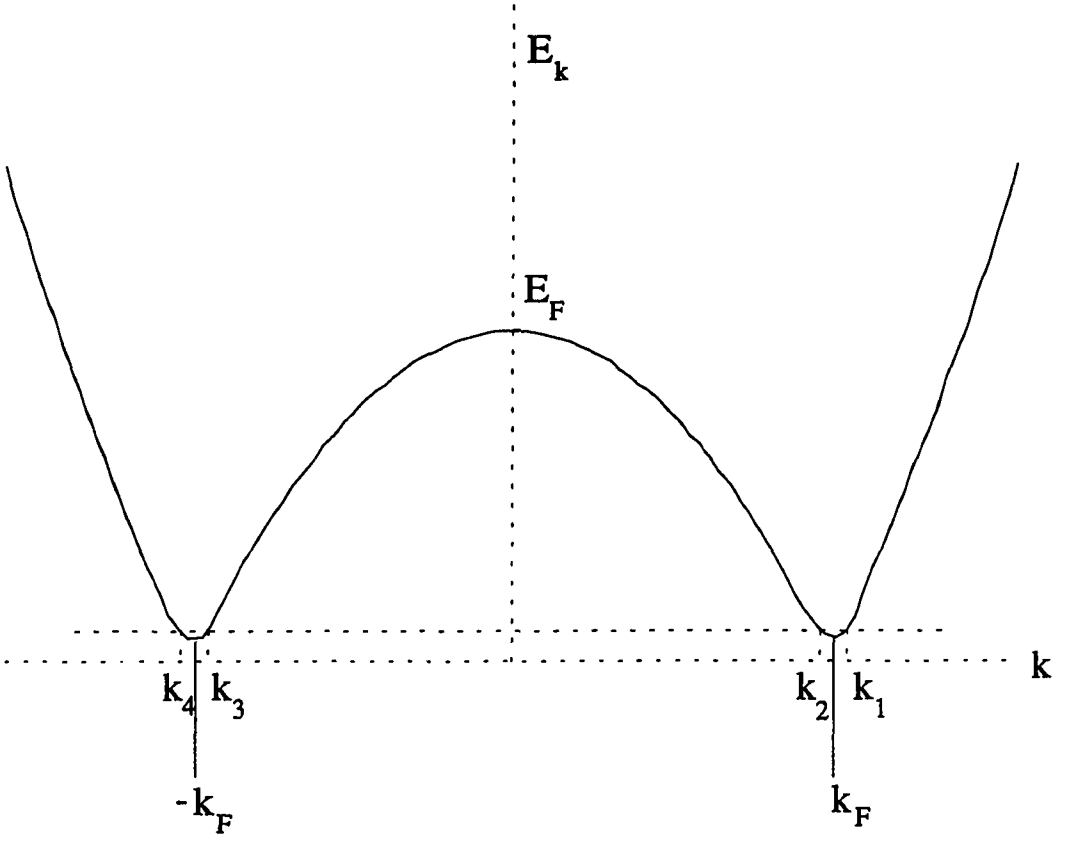

Figure 35. The energy diagram for the quasiparticles. The superposition of the four possible quasiparticle states above and below the Fermi surface give rise to a standing wave solution to the density of states within the electrical leads connecting the Josephson junction.

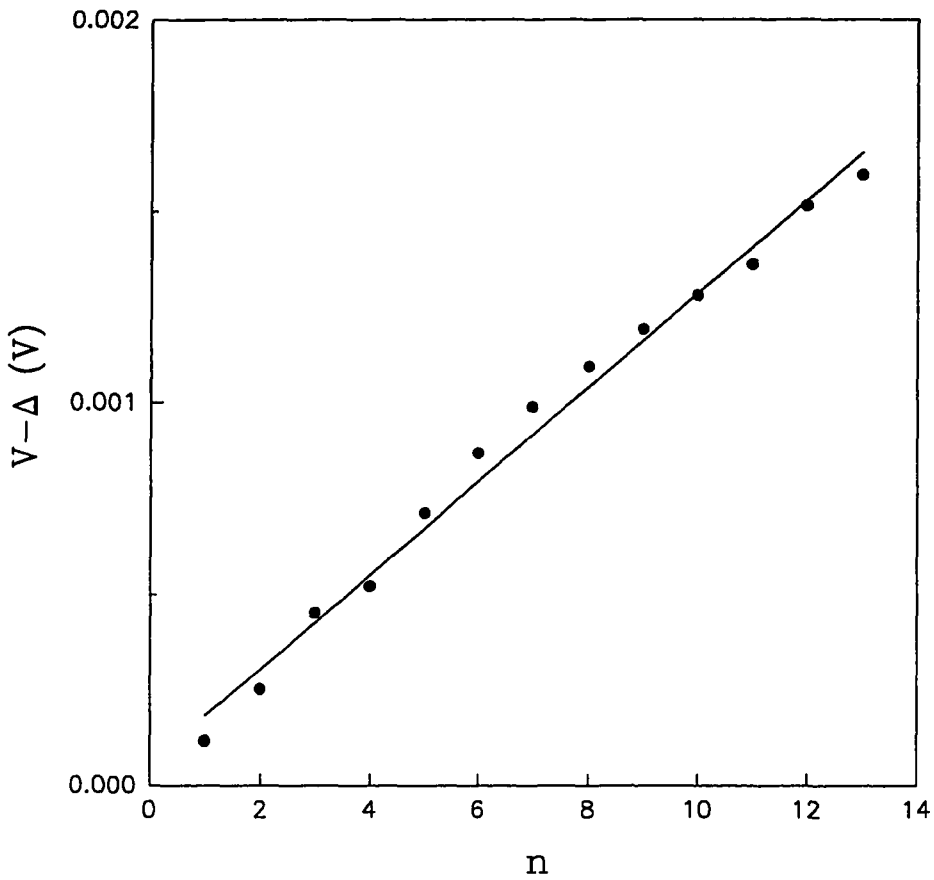

Figure 36. The voltage V-Δ of the staircases are plotted against the index number n. The slope of the line is given by $\pi\hbar v_F/d$. The experimental value of $1.22x10^{-4}$ is in reasonably agreement with the calculated value of $7x10^{-5}$.

IV.VI Electrical Environment

Because of the high frequency of the Bloch oscillations, there were some experimental evidence[19] on the effects of local electrical environment on the IV characteristics of the devices undergoing Bloch oscillations. The theories[15,16,17,18,20] on electrical environment suggest that it acts as an additional source of dissipation.

The electrical environment manifests itself through the parasitic capacitance C and inductance L of the electrical leads connecting the devices to the outside world. For a device connected to the outside world with low resistance leads, the electrical environment smears Coulomb gap by introducing fluctuations of the order $2\pi\hbar/\sqrt{LC}$. In that sense, the electrical environment contributes to the overall dissipation of the junctions undergoing Bloch oscillations.

In order to account for the effects of electrical environment on the IV characteristics of the chains, we have fabricated chains with two different lengths with different inter-junction separations. In addition, all devices measured were electrically isolated by high resistance metal film resistors. Figure 37 shows the dynamic resistances of two linear chains of two different inter-junction distances with identical normal state resistances of 3.3 KΩ; the 12 junction chains had an inter-junction distance of 9 μm, and the 164 junction chain has an inter-junction separation of 2.5 μm. The change in inter-junction distance translates roughly into a change of a factor of three in the inductance of the leads. Yet, no major differences in the dynamic resistances were observed insofar as the width and the height of the zero bias peaks are concern.

The electrical isolation of the devices was achieved by inline metal film resistors mounted as close to the devices as possible. These inline resistors, together with the parasitic capacitances and inductances of the wiring, give rise to additional time constants RC and L/R to smear the coulomb gap. However, no significant changes in the IV characteristics were ever observed over all temperature ranges when the values of the inline resistors were varied over five orders of magnitudes, from 500 KΩ to 100 Ω. The

result was not very surprising ; if the inline resistors were affecting the device characteristics at all, they would affect only the outermost junctions, which only made a minuscule contribution to the overall characteristics of the chains. The parasitic capacitance and the inductance of the insert seen at the outermost junction of the chains were estimated to be 0.5 fF and 10 pH, respectively.

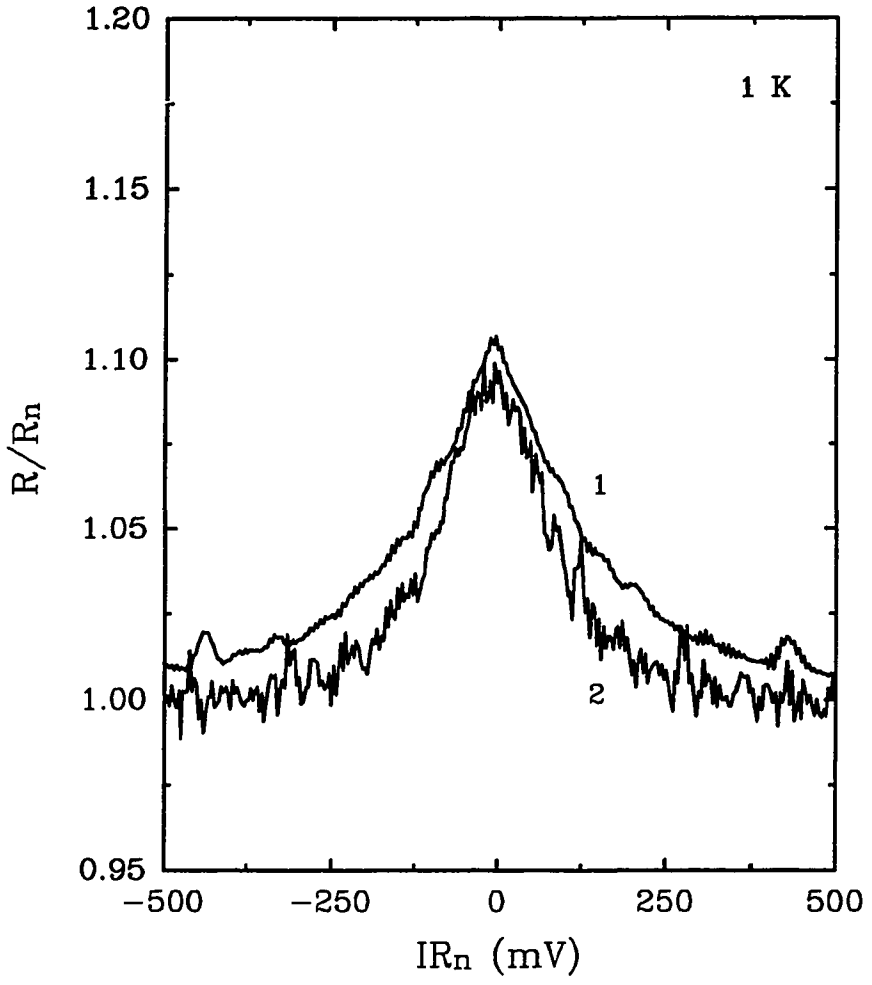

Figure 37. The dynamic resistances of **1.** 12 and **2.** 164 junction chains. Both chains have identical normal state resistance of 3.4 KΩ. The measurements were taken at 1 K, and the superconductivity was quenched by magnetic field. The upper curve was slightly displaced upward for clarity.

IV.VII Summary

The data on the linear chains suggests that the quasi-reentrant behavior may be the result of competition of quasiparticle and supercurrent conduction. In addition, the presence of charge traps within the tunneling barriers modulate the junction dynamic resistance, causing junction dynamic resistance to fluctuate as charged carriers hops in and out of the charge traps.

Because of the high frequency of the Bloch oscillations, the electrical environment manifests itself through the parasitic capacitance C and inductance L of the electrical leads connecting the devices to the outside world. For a device connected to the outside world with low resistance leads, the electrical environment smears Coulomb gap by introducing fluctuations of the order $2\pi\hbar/\sqrt{LC}$.

In order to account for the effects of electrical environment on the IV characteristics of the chains, we have fabricated chains with two different lengths with different inter-junction separations to account different inductances and varied the inline isolation resistors to account for effects by the parasitic capacitance's of the systems. No significant changes in the IV characteristics were ever observed over all temperature ranges. The effects of electrical environment on the IV characteristics were probably minimal at best.

However, the electrical leads do more than just smears the Coulomb gap. Quasiparticles often exhibit long range coherence within long electrical leads. This effect is purely the consequence of the presence of the superconducting parameter and the phase coherence of the superconducting ground state.

In many instances, quasiparticles behave much like normal electrons. However, normal electrons do not exhibit the long range coherence of the quasiparticles. The effects of long range quasiparticle coherence become significant in long electrical leads, such as the ones connecting the ultra small tunnel junctions to the electrical contact pads in the

devices studied. The long range coherence of the quasiparticles manifest themselves as discrete steps in the IV characteristics of the Josephson junctions.

Another aspect of the data is the appearance of the dynamic resistance oscillations. Such oscillations have also been observed by the author in linear chains. The source of the oscillations is not known. However, two possibilities exist:

1. The oscillations are believed to be caused by the presence of charge traps within the tunneling barriers, thus modulating the dynamic resistance of the tunnel junction as the traps captures and release electrons. The presence of the traps have been observed in devices studied.

2. The chain is highly disordered in the sense that junction resistances vary greatly from junction to junction within the chain. As a result, the junction become superconducting over a much wider temperature range than usual. Each of the dips in the resistances indicates a junction becoming superconducting as temperature was lowered.

In addition, measurements on the single junctions connected by long electrical leads showed that long range coherence of the quasiparticles in the leads can cause a series of steps to be developed in the IV characteristics of the device.

References

[1] B. G. Orr, H. M. Jaeger, A. M. Goldman and C. G. Kuper, *Phys. Rev. Lett.*, **56**, 378, (1986).

[2] B. G. Orr, H. M. Jaeger and A. M. Goldman, *Phys. Rev. B*, **34**, 4920, (1986).

[3] M. Kuncher, P. Lindenfeld and W. L. McLean, *Phys. Rev. Lett.*, **59**, 1233, (1987).

[4] A. E. White, R. C. Dynes and J. P. Garno, *Phys. Rev. B*, **33**, 3549, (1986).

[5] M. A. Fisher, thesis, unpublished.

[6] A. Barone, G. Paternò, *Physics and Applications of the Josephson Effect,* Chapter 6, 121, (1982).

[7] M. C. King and M. R. Goldrick, *Solid State Technol.*, **19.2**, 37, (1977).

[8] J. D. Cuthbert, *Solid State Technol.*, **20.8**, 59, (1977).

[9] J. S. Greeneich, *J. Elecrochem. Soc.*, **122.7**, 970, (1975).

[10] M. Hatzakis, C. H. Ting, N. Viswanathan, *Intl. Conf. Electron Ion Beam Sci. Technol., 6 th,* 542, (1974).

[11] R. J. Hawryluk, A. M. Hawryluk, H. I. Smith, *J. Appl.Phys.*, **46.6**, (1974).

[12] K. Mullen, E. Ben-Jacob, R. C. Jacklevic and Z. Schuss, *Phys. Rev.* B, **36**, 98, (1988).

[13] W. L. McMillan and P. W. Anderson, *Phys. Rev Lett.*, **16**, 85, (1965).

[14] A. C. Anderson, *Rev. Sci. Instrum.*, **44**, 1475, (1973).

[15] M. Girvin, L. I. Glazman, M. Johnson, D. R. Penn and M. D. Stiles, *Phys. Rev. Lett.*, **64**, 3183, (1990).

[16] M. H. Devoret, D. Esteve, H. Grabert, G. L. Ingold, H. Pothier and C. Urbina, *Phys. Rev. Lett.*, **64**, 1824, (1990).

[17] Yu V. Nazarov, *Sov. Phys.* JETP, **68**, 561, (1989).

[18] G. L. Ingold and H. Grabert, *Europhys. Lett.*, **14**, 371, (1991).

[19] A. N. Cleland, M. J. Schmidt and J. Clarke, *Phys. Rev. Lett.*, **64**, 1565, (1990).

[20] G. Schön, "*Influence of the Electromagnetic Environment on the Charge Dynamics of Small Tunnel Junctions*", preprint, (1991).

[21] D. V. Averin and K. K. Likharev, *Journal of Low Temperature Physics*, **62**, 345 (1986).

Vita

Joseph J. Tien was born on March 8, 1960 in Taipei, Taiwan. He received his B.S. in Chemical Engineering and Applied Physics from University of California at Berkeley in 1983. He has subsequently received his M.S. in Physics from UCLA in 1985, and his Ph.D. in Physics from University of Illinois at Urbana-Champaign in 1994.